Experimental reproduction of the martian weathering profiles argues for a dense Noachian CO2 atmosphere

Jean-Christophe Viennet, Benjamin Bultel, Stephanie C Werner

▶ To cite this version:

Jean-Christophe Viennet, Benjamin Bultel, Stephanie C Werner. Experimental reproduction of the martian weathering profiles argues for a dense Noachian CO2 atmosphere. Chemical Geology, 2019, ⟨10.1016/j.chemgeo.2019.07.009⟩. ⟨hal-03127691⟩

HAL Id: hal-03127691
https://hal.science/hal-03127691v1

Submitted on 1 Feb 2021

Experimental reproduction of the martian weathering profiles argues for a dense Noachian CO_2 atmosphere

Jean-Christophe Viennet[a]*, Benjamin Bultel[a], Stephanie C. Werner[a]

[a] Centre for Earth Evolution and Dynamics, Department for Geosciences, University of Oslo, Postboks 1028 Blindern, 0316 Oslo, Norway

Now at Muséum National d'Histoire Naturelle, Institut de Minéralogie, Physique des Matériaux et Cosmochimie, CNRS UMR 7590, Sorbonne Université, CNRS, F-75005 Paris, France.

* Author to whom correspondence should be addressed:

Jean-Christophe Viennet

Email address: jean.christophe.viennet25@gmail.com

Centre for Earth Evolution and Dynamics, Department for Geosciences, University of Oslo, Postboks 1028 Blindern, 0316 Oslo, Norway.

Abstract

On Mars, mineral sequences have been detected and they are composed of a top layer of Al-rich clay minerals, then (Al, Fe)-rich clay minerals and a bottom layer composed of (Mg, Fe)-rich clay minerals. By analogy with Earth, such sequences are interpreted as weathering profiles formed by the interaction of acidic solutions in equilibrium with the atmosphere and the parent rock. Thus, understanding of the aqueous solution composition leading to the above mineral description allows deciphering the atmosphere composition. We designed an experimental column system with three levels containing powdered basaltic rock to test the influence of different acidic fluids on the mineralogical formation. Five solutions were used: H_2SO_4 and HCl at pH 3 in equilibrium with N_2 atmosphere, pure water in equilibrium with 0.1 and 1 atmospheric pressure CO_2 leading to pH values of 3.9 and 4.4, respectively and a H_2SO_4 solution at pH 3 in equilibrium with 0.1 atmospheric pressure CO_2 leading to a pH value of 2.98. The results obtained show that the content of Al-rich clay minerals and the evolution from Al, (Al, Fe) to (Fe, Mg)-rich clay minerals formed are better reproduced with an originally high pCO_2. Hence, we suggest that acidic alteration driven by a dense CO_2 atmosphere reproduced better the observed martian weathering profiles. The experiments involving CO_2 led to the formation of carbonates. Their identification by near infrared (NIR) detection methods is challenged, because even the laboratory NIR spectra acquired on the experimental products show that: (i) the absorption bands related to carbonates are very weak, and (ii) the strongest feature at 3.95 µm is beyond the CRISM NIR range. Such carbonate formation is consistent with the recent carbonate detection at a planetary scale in weathering profiles, which goes toward that the weathering profiles could have been formed under a dense CO_2-rich atmosphere as suggested also by climatic models.

Key words

Mars, Clay Minerals, Carbonates, Column Experiments, Weathering Profiles, Atmosphere.

Highlights

- Martian weathering profiles (MWP) are simulated in open system column experiments.
- CO_2 rich fluid better reproduces the clay mineralogy observed in MWP.
- Carbonates should be present in MWP but their detection are challenging with NIR.
- Experimental investigation of early Mars suggests a dense CO_2-rich atmosphere.

1. Introduction

Widespread weathering profiles have been observed on the martian surface older than ~3.7 Gyrs (Carter et al., 2015). From top to bottom, they are composed of an evolutionary sequence from Al-rich clay minerals (kaolins and smectites), then $(Al,Fe)^{3+}$-rich clay minerals (mainly smectitic), to finally Fe,Mg-rich clay minerals (mainly smectitic) (Carter et al., 2015; McKeown et al., 2009). These alteration sequences were formed by weathering and they are remarkably consistent with clay mineralogy observed in soil profiles developed from basaltic rocks on Earth (Gaudin et al., 2011). Recently, carbonates have been detected in the middle section of weathering profiles (Bultel et al., 2019). High resolution images across these sequences suggest the absence of unconformities (Carter et al., 2015; Michalski et al., 2013), which exclude a two-steps process where first Fe/Mg-rich clay minerals were formed and then a Al-rich clay minerals were deposited. Finally, the sequences are widespread over the equatorial to mid-latitudinal regions of Mars, which argues for a regional to planetary scale climatically controlled formation process (Carter et al., 2015).

The formation of weathering profiles implies the presence of surface liquid water. Several modelling studies have evaluated the possibilities to sustain liquid water by evoking a sufficient greenhouse effect on Early Mars (Forget et al., 2013; Halevy and Iii, 2014; Kerber et al., 2015; Ramirez, 2017; Wordsworth, 2016; Wordsworth et al., 2017). CO_2 and H_2O gasses appear to be the main gasses causing a rise of the mean surface temperature, but their sole contribution appears to be insufficient (Wordsworth, 2016). Other possibilities have been explored to episodically warm up the martian surface requiring the presence of SO_2, H_2, CH_4 with CO_2 gas. Finally, even if at the present time there is no clear and definitive solution to explain the presence of liquid water on Mars, the different climatic simulations tend toward a CO_2-rich and dense atmosphere of up to 0.5-2 bars with potentially other greenhouse gasses to a lesser extent (from ppm to few percent).

Weathering as an acidic chemical process appears to be the most reasonable pathway for the formation of the clay mineral sequence (Zolotov and Mironenko., 2007; Farrand et al;, 2008; Gaudin et al., 2011; Michalski et al., 2013; Dehouck et al., 2014a; Farrand et al., 204; Zolotov and Mironenko, 2016; Gaudin et al., 2018, Peretyazkho et al., 2018; Bultel et al., 2019). The acidic solutions leading to the formation of the weathering profiles are a key to better understand Early Mars. They represent the link between the weathering profiles and the martian atmosphere during this epoch. Various chemical compositions have been put forward leading to the formation of the mineralogical sequences as S-bearing solution or CO_2-rich fluids.

S-bearing solutions have been proposed in experimental hydrothermal studies (Peretyazkho et al., 2018) and geochemical simulations (Zolotov and Mironenko, 2016). In their study, Zolotov and Mironenko (2016) used geochemical simulations with different acidic solutions composed of CO_2 and H_2SO_4-HCl acids to reproduce the mineral sequence of the martian weathering profiles. Because so far no carbonate has been detected in these martian sequences, Zolotov and Mironenko (2016) concluded that: “Weathering by low - pH H_2SO_4 - bearing solutions is more consistent with observations than alteration by S-free fluids”. The pH dependencies on clay mineral formation from basaltic glass hydrothermal experiments in closed system at 200°C show that H_2SO_4 acid at pH ~ 3 leads to the formation of dioctahedral smectite and sulfate, while at higher pHs, trioctahedral smectite and sulfate are formed (Peretyazhko et al., 2018) . Peretyazhko et al., (2018) also argue for a SO_2-rich atmosphere on Early Mars, which should inhibit carbonate formation as proposed by previous studies (Halevy et al., 2007; Bullock and Moore, 2007; Fernández-Remolar et al., 2011).The patchy occurrences of sulfates at Marwth Vallis (one of the martian weathering profiles) can be explained by the weathering with H_2SO_4 fluids (Bishop et al., 2013; Michalski et al., 2013; Farrand et al., 2014; Zolotov and Mironenko, 2016). Nevertheless, the patchy presence of sulfates can also be due to localized alteration postdating the formation of the weathering profiles (Altheide et al., 2010). In addition, S-bearing gasses would also lead to the end of warm conditions necessary to sustain liquid water at the surface (Kerber et al., 2015).

The hypothesis of CO_2 weathering fluids has also been investigated by chemical modelling and experimental studies. Zolotov and Mironenko (2016) show that the clay minerals evolution can be reproduced but even with the presence of H_2SO_4 acid in solution, carbonates should form in the weathering profiles at depth where the pH is neutral due the dissolution of the basaltic rock. Dehouck et al., (2014a) and Gaudin et al., (2018) have performed experiments of weathering of olivine at different water rock ratio (evaporitic and 10) and duration (from 45 to 470 days) at 45°C under 1 bar of CO_2 or air atmosphere. For both studies, Fe,Mg smectite can form under such conditions. Also, for the longest experiments with a water rock ratio of 10, they observed the formation of Al-rich clay minerals. They conclude that the Al-rich upper horizons of the weathering profiles can form under a CO_2 dense atmosphere even if the parent material is poor in aluminum. In such condition, carbonates have formed. Such hypothesis appeared counterintuitive as carbonates have not been observed in the martian weathering profiles at that time. Yet, such atmosphere is more favorable to sustain liquid water on the surface of Mars (Wordsworth, 2016).

Based on this, no consistent conclusion can be drawn. In order to provide additional constraints on the acidic solutions, the present study aims at investigating the scenarios proposed, which could lead to the martian weathering profiles. The acidic scenarios (i.e. acidic event driven by H_2SO_4, HCl and/or CO_2) have been evaluated using a setup dedicated to mimicking the martian weathering profiles. We designed an open column system consisting of three stacked shelves where the solution passes through from bottom to top. In order to decrease the experiment duration, the experiments were performed at 150°C and the water is kept liquid in the system via a backpressure regulator set at 5 bars. The consequences of such higher temperature on the mineral formation are discussed in section 4.2.1. Five acidic solutions were used: pure water in equilibrium with 1 and 0.1 pCO_2 leading to pH values of 3.9 and 4.4 respectively, H_2SO_4 and HCl acidic solution at pH 3 in equilibrium with 1 pN_2 and finally H_2SO_4 solution at pH 3 in equilibrium with 0.1 pCO_2 leading to pH value of 2.98. The mineral formation pathways are investigated through the cationic composition and the pH measurements of the output solutions. In addition, solid analyses by using X-Ray Diffraction (XRD) and near-infrared (NIR) measurements were performed to characterize the alteration products. The obtained results show that acidic fluids rich in CO_2 better reproduce the general trend of the weathering profile sequence. Finally, we suggest that the mineralogical weathering profile observations could have been formed through acidic weathering in a dense CO_2-rich atmosphere in accordance with the recent carbonate detection in these weathering profiles (Bultel et al., 2019).

2. Materials and Methods

2.1. Sample selection and preparation

The basaltic powder used for the experiments was prepared from a volcanic basaltic glass of tholeiitic composition from Iceland (Stapafell, Reykjanes Peninsula, Iceland). Particle sizes of less than 10 µm were crushed by micronizing (for more details see Viennet et al. (2017)) and used to conduct the experiments. The chemical composition of the final powder has been obtained by fusion and XRF analysis (Actlabs, Canada, Table 1). The chemical composition of the basaltic glass is in the range of the chemical composition range of the martian surfaces (Bell, 2008) and from the in-situ measurements of basaltic rock at Gusev Crater (McSween et al., 2006). Basaltic glass was chosen because it has the highest rate of dissolution compared to the crystalline basaltic minerals (Gislason and Hans, 1987; Gislason and Arnórsson, 1993; Gislason et al., 1996; Stefánsson et al., 2001) leading to a decrease of experiments duration. Also, volcanic glass has been measured as one of the main component of the rocks analysed with the Curiosity rover on Mars (Bish et al., 2013; Meslin et al., 2013; Dehouck et al., 2014b; Smith et al., 2018).

2.2. Experimental set up and procedure

The experiments were performed in a newly-developed open system column with three stacked shelves for the rock powders to mimic the natural weathering process. The technical sketch of the experimental setup is presented in Figure 1. One liter of input aqueous solution was flushed with the desired gas for 10 min. Then, the input aqueous solution was put in equilibrium with the same desired gas composition at atmospheric pressure and that throughout the experiment. Five different experiments were performed, which correspond to five input aqueous solutions in equilibrium with the considered gas at 20°C and 1 bar (Table 2). Two of them were performed with pure water equilibrated with either a gas composed of 100 % of CO_2 leading to an initial calculated pH value of 3.9 (referred as water - 1 pCO_2) or with a gas composed of 10% CO_2 (± < 1%) and 90% N_2 leading to an initial calculated pH value of 4.4 (referred as water - 0.1 pCO_2). Two solutions correspond to H_2SO_4 and HCl acidic water calculated and measured at pH 3 (±0.05) equilibrated with a gas composed of 100% N_2 (referred as H_2SO_4 - 0 pCO_2 and HCl - 0 pCO_2, respectively). The acidic solutions were prepared from standard 1 $mol.L^{-1}$ HCl or H_2SO_4 solutions diluted with pure water. The last experiment corresponds to an input solution composed of H_2SO_4 acid at pH 3 (±0.05) in equilibrium with a 10% CO_2 / 90% N_2 gas leading to an initial calculated pH value of 2.98 (referred as H_2SO_4 - 0.1 pCO_2). The initial pH values evolve before the alteration due the temperature dependency of pH (see below, the recalculated pH at 150°C). The aqueous solutions were injected in the column from the bottom via a high pressure liquid chromatography pump at a flow rate of 0.05 $mL.min^{-1}$ (± 5%). The column consists of a titanium cylinder and stainless steel tubing able to resist the acidic conditions. In order to decrease the time of reaction, the aqueous solution is heated to 150°C with a furnace around the column and kept liquid applying a 5 bars constant pressure in the system via a backpressure regulator. This pressure corresponds to the above water vapor limits pressure at such temperature. The initial pH value at 150°C and 5 bars were calculated using the EQ3/6 software (Wolery, 1992). Hence, the initial pH at 150°C and 5 bars of the water - 1 pCO_2 experiment is 4.1, for the water - 0.1 pCO_2 experiment is 4.6, for the H_2SO_4 or HCl - 0 pCO_2 experiments are 3.2 and for the H_2SO_4 - 0.1 pCO_2 experiment is 3.17 (Table 2). The input aqueous solutions were injected through the three rock powder holders, labelled level #1, #2 and #3 from bottom to top. Each holder contains 0.5 grams of basaltic glass powder at the start of the experiments. Each experiment was conducted for a period of 20 days and the output solution was collected every ~48 hours. After the 20 days of experiments, the furnace was turned off and the system cooled down to ~50°C within 4 hours. Then, the three holders with the altered materials are collected from the column. The three samples from each level were dried in an oven at 80°C (for around 10 h) prior to their characterization.

2.3. Aqueous solution analysis

2.3.1. Analytical measurements

Directly after the output solution sampling, the pH of the solution is measured at 20°C with an AgCl–KCl combination electrode calibrated at ~20°C with pH buffer solutions. The uncertainty for each measurement was ±0.05 pH units. Prior to the analytical measurements, the output solutions were filtered through 0.2 µm sterile cellulose nitrate filter. The Si concentrations were measured by cation chromatography instrument (Dionex ICS-2000) by a calorimetric method based on the reduction of silico-molybdate in acidic solution to “molybdenum blue” by ascorbic acid (Skougstad et al., 1978). The lower detection limit was 0.02 ppm and the maximum uncertainty was estimated at 5% based on reproducibility test. The Mg^{2+}, Ca^{2+}, Na^+ and K^+ concentrations were measured by cation chromatography with the Dionex ICS-1000 Ion Chromatography System. The detection limits for all elements were lower than 0.1 ppm and the maximum uncertainty was estimated at 5% based on reproducibility test. The Al and Fe concentrations of the input and output solutions were measured with an inductively coupled plasma mass spectrometry (aurora Elite Bruker) equipped with a Cetac ASX-250 autosampler and an ESI oneFAST sample introduction system. The detections limits were lower than 5 ppb and the uncertainty was estimated at 5%. The pH values at 150°C were calculated from the pH measurements at 25°C to take into account the ion concentrations and the chemical composition of the output aqueous solution by using the EQ3/6 software (Wolery, 1992).

2.4. Solids analysis

2.4.1 XRD analysis

XRD analyses were performed on the unreacted and the weathered samples for each experiment. Bulk analyses were performed on powder preparation. The DIFFRAC.EVA software with the PDF4 database has been used for the mineral identification. To determine the clay mineral nature on oriented preparation, each clay mineral sample was Ca- and K-saturated by using four saturation cycles of 0.5 $mol.L^{-1}$ of $CaCl_2$ and 1 $mol.L^{-1}$ of KCl (W/R = 200). Then, the samples were washed in distilled water and dried at 50°C. For each saturated sample, oriented preparations were performed by pipetting slurries of the particles dispersed in distilled water on glass slides and dried at room temperature (preparation referred as air dried -AD). The Ca-preparations were solvated by exposing the glass slides to ethylene-glycol vapor at 50°C overnight (Ca-EG). Concerning the K-saturated samples, each K-AD preparations were successively heated at, 110, 330 and 550°C in an oven for 4 hours. XRD acquisitions were obtained after each temperature step. The treatments are referred as K-110, K-330 and K-550. The XRD patterns were recorded on a D8 Advance Bruker (CuKα_{1+2} radiations) from 2 to 55°2θ using a step interval of 0.25°2θ and a counting time per step of 2.5 s. The size of the divergence slit, the two soller slits and the antiscatter slit were 0.25°, 2.5°, 2.5° and 0.5°, respectively.

2.4.2. Near infrared analysis

The near-infrared reflectance spectra were obtained with a PerkinElmer Fourier-transform infrared spectroscopy (FTIR) spectrometer from 1 to 4 µm wavelengths with a spectral resolution of 4 cm^{-1} at IAS-Orsay, France. The light source is a broadband source and the detector is a deuterated-triglycine sulfate detector. The spectrometer was calibrated by using *Spectralon* 99% (0.9 to 1.2 µm) and *Infragold* (1.2 to 4 µm) samples. The different spectra were acquired under ambient temperature and pressure conditions on the same powder preparations as for the bulk XRD analysis.

2.4.3. SEM-EDS analysis

All backscattered electrons pictures were obtained using a TESCAN VEGA II LSU scanning electron microscope at the Museum National d'Histoire Naturelle, Paris (Plateau Technique de Microscopie Electronique, PTME). The SEM observations were performed on carbon-coated samples with an accelerating voltage of 15kV. A silicon drift detector with a 133 eV resolution allowed us to perform energy dispersive X-rays spectroscopy in order to get qualitative information about the chemistry of the materials.

3. Results

3.1. Chemical elements release in the output solution

3.1.1. pH values and [H^+] consumption

The final pH values measured are higher than the initial pH values at 25°C (Figures 2.a - e). After 300 hours, the final pH values (20°C) are nearly constant through time and they increase with the decrease of pCO_2. The pH final values are circumneutral to alkaline (Figures 2.a, and Table 3). With the increase of pCO_2, the pH values (at 20°C) evolve from 6.35, 8.10, 8.32 to ~8.5 for the water - 1 pCO_2, water - 0.1 pCO_2, H_2SO_4, - 0.1 pCO_2 and 0 pCO_2 experiments, respectively (Table 3). Hence, the solutions containing CO_2 have not been completely neutralized and buffered by the rocks. The H^+ consumptions have been calculated by the difference between the initial and final pH values. The H^+ consumptions decrease with the pCO_2 increase (Figures 2.a - e). The same H^+ consumption can be noticed for the experiments with HCl and H_2SO_4 - 0 pCO_2. Consistently, the H^+ consumption of the H_2SO_4 – 0.1 pCO_2 experiment corresponds to the sum of the H^+ consumption for water - 0.1 pCO_2 and H_2SO_4 - 0 pCO_2 experiments. The pH values have been simulated for the experimental temperature 150°C and are presented in Figures 2.f - j and table 3. The values are nearly constant through times. They decrease with the pCO_2 increase but in a lesser extent than at 25°C due to the pH temperature dependence. The final pH values at 150°C are 6.07, 7.01, 6.88, 7.04, 7.02 for the water - 1 pCO_2, water - 0.1 pCO_2, H_2SO_4 - 0.1 pCO_2 and 0 pCO_2 experiments, respectively (Table 3).

3.1.2. Composition of the output solution

The Figures 3.a - e present the total quantities in mol of the main chemical elements released in the output solutions from the original basaltic glass dissolution. The quantities of Si released increase with the increase of pCO_2. The values of Si released (comprised between 3.1 and $9.6 \cdot 10^{-3}$ mol at the end of the experiments) are the highest compared to the other chemicals elements. Mg^{2+} is released for the sole water - 1 pCO_2 experiment ($9.6 \cdot 10^{-4}$ mol at the end of the experiment, Fig. 3.b). The highest Ca^{2+} quantities released is for the water - 1 pCO_2 experiment ($2.0 \cdot 10^{-3}$ mol at the end of the experiment, Fig. 3.c). The Ca^{2+} values of the experiments involving H_2SO_4 acid are similar (1.1 and 1.3 10^{-3} mol, for the 0 pCO_2 and 0.1 pCO_2, respectively, at the end of the experiments) and the Ca^{2+} values for the water - 0.1 pCO_2 and HCl - 0

pCO_2 experiments are alike and the lowest (respectively, 7.7 . 10^{-4} and 9.4 . 10^{-4} mol at the end of the experiments, Fig. 3.c). The quantities of Na^+ and K^+ released (comprise between 1 and 7 . 10^{-4} mol at the end of the experiments) are lower than for Ca^{2+} and Si and the values are similar among the experimental conditions (Fig. 3). The Al and Fe values are not shown, because they are two orders of magnitudes lower than the Si values, despite that they are of about the same order of magnitude in the structure of the original basaltic glass (see table 1).

The Figures 3.f, g, h and i show the Mg/Si, Ca/Si, Na/Si and K/Si ratios of the elements released in the output solutions and of the unreacted material. For all experiments after 300 hours, the chemical ratios of the output solutions are constant. The Mg/Si ratios are null except for the water - 1 pCO_2 experiment (value of 0.1), for which the Mg/Si ratio is lower than for the unreacted material (ratio of 0.29, Fig. 3.f). The Ca/Si ratios for the HCl and H_2SO_4 - 0 pCO_2 experiments are slightly above the Ca/Si ratio of the unreacted material (Fig. 3.g), while the Ca/Si ratios of the experiments involving CO_2 (the ratios are at the end of the experiments: 0.21, 0.14 and 0.19 for the water - 1 pCO_2, water - 0.1 pCO_2 and H_2SO_4 - 0.1 pCO_2 experiments, respectively, Fig. 3.g) are lower than the unreacted material ratio (value of 0.26, Fig. 3.g). For the Na/Si and K/Si ratios for all experimental conditions, the ratios are those of the pristine material ratio (respectively values of 0.07 and 0.01, Fig. 3.h and i). These low output solution ratio variations are due to the formation of the corresponding secondary minerals as functions of the initial conditions. Finally, the chemical ratios and the pH of the output solutions are constant after 250 hours (Fig. 2 and 3), which indicates that the reactions achieved solid-solution equilibration.

3.2. Characterization of the solid samples

3.2.1. Characterization of the unreacted sample

Figure 4 presents the XRD pattern and NIR spectrum obtained on the pristine material. The XRD pattern exhibits a large and high bump between 5 - 2.33 Å and centered at 3.23 Å corresponding to basaltic glass. Minor minerals (<10 %, SEM measurements see figure S2 and Gysi and Stefánsson (2012a)) can also be identified by XRD peaks (Figure 4) such as quartz (triangles), olivine (diamonds) and pyroxene (squares). The NIR spectrum (Figure 4) highlights the presence of olivine (diamonds) (Cloutis et al, 1986) and pyroxenes (squares) at 1 µm (Adams, 1974; Cloutis et al, 1986) as the basaltic glass and quartz are not visible in such NIR range. The absorption bands at ~2.82 µm correspond to water molecules probably adsorbed on the basaltic particles. The SEM measurements have shown that the olivine is close to the chemical composition of forsterite (Figure S2.c). The pyroxene is close to the chemical composition of augite (Figure S2.c). Small patch of chromite also have been detected in inclusions of the glass and forsterite (Figure S2.a and c). The main phase carrying Fe is the basaltic glass, since the proportion of augite and chromite is low in the bulk material. In such basaltic glass, Fe is present in the oxidation degree II (Christie et al., 1986; Gysi and Stefánsson, 2012a). Quartz cannot be found in such basaltic rocks and its presence is interpreted as a contamination during the filed collection.

3.2.2. Characterization of the reacted samples

The XRD patterns of the reacted samples are presented in Figure 5. Compared to the pristine material, the intensities of the XRD peaks corresponding to the basaltic glass decrease and new XRD peaks and absorption bands appear. These indicate that the basaltic glass was dissolved and new minerals formed (Figure 5). Quartz, forsterite and augite are not dissolved during the experiment because their XRD intensities are similar to the pristine material. In such conditions, the percentage of dissolution of the basaltic glass can be obtained by using the full pattern fitting method (Chipera & Bish, 2013; Viennet et al., 2017). This method consists of determining the difference in area between the XRD peaks corresponding to both the original glass and the altered sample. Preliminary tests have been performed on laboratory mixtures for various proportions of basaltic glass and zinc. The results show that the content of glass can be determined with an accuracy of ±2.5%. The results obtained on experimental residues are presented in the Table 3. For a given experimental condition, the percentage of dissolution decreases with the increase of level #. Also, the percentage of dissolution increases with the increase of pCO_2.

Concerning the non-clay mineral formation, the XRD peaks at 3.00, 2.84, 2.5, 2.01, 1.99 and 1.98 Å (Figure 5) and the absorption bands at 3.85 and 3.95 µm (Figure 6) exhibit the presence of calcite (Hunt and Salisbury, 1971; Cloutis et al., 2003) at the three levels of the water - 0.1 pCO_2 experiment. Ca-Mg-Fe carbonates are noticed by the 3.0 and 2.1 Å peaks and the absorption band at 3.85 and 3.95 µm for the level #2 and #3 of the H_2SO_4 - 0.1 pCO_2. The water - 1 pCO_2 experiment exhibit XRD peaks at 3.0 Å and 2.01 Å and absorption bands at 3.85 and 3.95 µm only present for the samples of level #3 indicating Ca-Mg-Fe carbonate. Interestingly, boehmite (AlO(OH)) can be observed with the XRD peaks at 6.1 Å only for the sample of level #1 of the H_2SO_4 - 0.1 pCO_2 experiment (Figure 5).

As far as clay minerals are concerned, 00*l* and 020 reflections of clay minerals can be noticed. A detailed characterization of the XRD patterns dedicated to clay mineralogy can be found in supplementary information (text and Figures S2, S3, S4, S5, S6 and S7). Briefly, the irrational 00*l* reflections at 14.4 and 2.6 Å correspond to a random (R0) smectite/chlorite mixed-layer mineral (MLM). The irrational 00*l* reflections at 7.2, 3.5, 2.4 and 1.99 Å correspond to a R0 Fe-rich chlorite/smectite MLM. With the increase of pCO_2 or with the decrease of level #, the content of the R0 Fe-rich chlorite-smectite MLM increase relatively compared to the R0 smectite/chlorite MLM. The clay minerals formed and their evolution with the pCO_2 are in line with previous experiments performed in closed systems on the same basaltic rocks (Viennet et al., 2017). In addition, the 020 reflections of the clay minerals shift from 4.49 to 4.59 Å with the pCO_2 decrease and the increase of level #. Similarly, a slight shift can also be noticed on the 060 XRD patterns (Figure S1). Such behavior could be assigned to an evolution from dioctahedral to trioctahedral structure. In order to better identify these evolution, NIR spectrum with continuum removed between 2.1 and 2.5 µm are presented in Figure 7. Note that, the characterization of the octahedral evolution on the martian weathering profiles is also made in this spectral range.

3.2.3. Octahedral characterization of the clay minerals formed

The XRD identification has shown that the minerals present in the samples are a mixture of R0 Fe-rich/smectite MLM and R0 smectite/chlorite MLM. The NIR spectra confirm the presence of smectite and chlorite by their characteristic adsorption bands at 1.41 and 1.91 µm corresponding to the bending and stretching overtone of bond water and between 2.19-2.5 µm corresponding to cation-OH bond (Figures 6 and 7) (Bishop et al., 1994; Clark et al., 1990; Hunt and Salisbury, 1970).

The XRD identification (see supplementary file and section 3.2.2) shown that with the pCO_2 increase and the level #, the content of the R0 Fe-rich/smectite MLM increase relatively to the R0 smectite/chlorite MLM. The NIR measurements show a similar tendency as the adsorption bands at 2.31-2.35 decrease relatively compare to the adsorption bands at 2.19 and 2.25 µm. Indeed, regarding the level #1 of the water - 1 pCO_2 experiment, the XRD identification shows that the residue is manly made of a R0 Fe-rich chlorite/smectite MLM. The adsorption bands at 2.19 and 2.25 µm of the NIR spectrum are the highest for this sample (Figures 6 and 7). This bands are related to Al_2-OH and $(Al,Fe)_2$-OH bonds of dioctahedral smectite and or chlorite (Clark et al., 1990). Hence, the combined XRD and NIR measurements confirm that this mineral is a dioctahedral R0 Fe-rich chlorite-smectite MLM. Also, the NIR measurements show adsorptions bands at 2.31 and 2.35 µm. These bands are mainly present in the CO_2 free experiments. The XRD interpretations have shown that the main clay mineral is a R0 smectite/chlorite MLM. The NIR bands at 2.31 can be related to $(Fe,Mg)_3$-OH stretching and bending bands of trioctahedral smectite. Also, the absorption band at 2.35 µm could correspond to $(Fe,Mg)_3$-OH in Fe-rich trioctahedral chlorite (Figure 7.c and d) (Bishop et al., 2008; King & Clark, 1989, Clark et al., 1990). Hence, this mineral is a trioctahedral R0 smectite-chlorite MLM.

For all experiments, the absorption bands depths decrease with the increase of the level # (Figure 7). This indicates that the amount of clay minerals formed decreases. As noticed by the XRD and NIR mineral identification, the octahedral (i.e. di- to trioctahedral) composition of the R0 MLM changes as function of the experiments. This can be followed by the respective absorption band depth ratio between Al_2-OH + $(Al,Fe)_2$-OH bands and $(Fe,Mg)_3$-OH bands (Figure 8.a). With the increase of level #, the dioctahedral bonds decrease in favor of the trioctahedral bonds in clay minerals as noticed by the di/tri ratios decrease (Figure 8.a). Finally, more $(Fe,Mg)_3$-OH bonds are present in the clay minerals formed in the upper levels (Figure 8.a). In addition, more dioctahedral clay minerals are formed with the pCO_2 increase as the increase of the di/tri ratios values for a same level # shows (Figure 8.a). Finally, the evolution from Al_2-OH to $(Al,Fe)_2$-OH bonds in the octahedral sheet of clay minerals can be experimentally investigated by following the respective absorption band depth ratios between the Al_2-OH and Al_2-OH + $(Al,Fe)_2$-OH bands (Figure 8.b). The highest $Al_2/(Al_2+[Al,Fe]_2)$ ratio is measured in the 1 pCO_2 experiment. In addition, the ratios decrease gradually from level #1 to #3 but never reach null value. In all other experiments, the ratios exhibit null values along the column and a non-regular decrease of the ratios as a function of the level #. This evolution is due to the predominance of Al_2-OH bands for the 1 pCO_2 experiments compared to the other experiments where such absorption band is fairly weak. Table 3 gives an overview of the mineral identification and evolution highlighted by the XRD and NIR measurements.

4. Discussion

4.1. Effect of the acid used on the evolution of geochemical conditions and minerals formation

For all of the experimental conditions, the decrease of dioctahedral bonds in favor of trioctahedral ones with the increase of level # (Figure 8.a, table 3) can be related to the pH increase due to dissolution along the column system (Table 3). Indeed, the octahedral composition evolves with the pH of alteration. The pH dependency was evaluated by experiments and geochemical modelling in closed systems with basaltic glass of similar composition (Peretyazhko et al., 2018; Viennet et al., 2017) and by numerical models on basaltic rock of similar composition (Zolotov and Mironenko, 2016). These studies show an increase of dioctahedral clay mineral formation with the decrease of pH. The rock powder present in the level #1 is reacting at the initial acidic pHs, which are the lowest in the column experiments. Hence, the minerals formed are enriched in Al_2-OH and (Al,Fe)-OH. In the levels above (second and third), more Mg^{2+}

is incorporated in the octahedral sheet of the clay mineral structure due to the increase of pH by the buffering of the basaltic glass dissolution (Table 3 and Figure 8.a).

With the increase of pCO_2, the dissolution of the basaltic glass increases as shown by the increase of percentage of dissolution by XRD (Table 3) and hence highest Si quantities are released (Figure 3). This evolution argues for lower acidity during the alteration with the increase of pCO_2 (Table 3). This is in accordance with the fact that basaltic glass dissolution increases with the pH decrease (Oelkers and Gislason, 2001; Gislason and Oelkers, 2003; Strachan, 2017 and references therein). Nevertheless, the initial pH values are higher for the water - 1 and 0.1 pCO_2 experiments compared to the HCl/H_2SO_4 - 0 pCO_2 experiments. Gysi and Stefánsson (2011) noticed, by performing numerical simulation for closed systems, that with increasing pCO_2, the system is shifted towards the CO_2 - basalts buffered alteration system and it requires more time and dissolved basaltic glass to reach pH values >8, as for the zero pCO_2 experiments. This evolution was also noticed by Viennet et al. (2017) performing closed systems experiments on basaltic glass dissolution for the same duration of reaction. The continuous renewal of the input solution the pH of the solution is too low for the formation of carbonates in the two first layers of the water - 1 pCO_2 experiment. The lack of carbonates means that CO_2 fluids are not buffered by the basaltic glass in the first layers, so low-pH solutions penetrate more efficiently to the next less altered solids. In the experiments free of CO_2, the pH is not controlled by CO_2 buffering but by the buffering of the basaltic glass itself. As the reactivity of basaltic glass is high upon dissolution (Gislason and Hans, 1987; Gislason and Arnórsson, 1993; Gislason et al., 1996; Stefánsson et al., 2001), the increase of pH is important. Hence, the final pH values are lower for the CO_2 experiments than for the CO_2-free experiments even though the initial pH values of the experiments involving CO_2 are higher.

In acidic conditions, alkaline cations such as Mg, Ca, Na and K are more mobile than Al, Fe and Si (Martini and Chesworth, 2013; Mason and Moore, 1982; Pedro and Delmas, 1970). Such evolution driven by the initial experimental conditions is supported by the investigation of the chemicals elements released in the output solution. Of note, no SiO_2 formation and dissolution were measured during the experiments.

Despite the fact that Ca is a mobile cation in acidic conditions, the Ca/Si ratios in the output solutions are highest for the CO_2-free experiments, while the final pH values are the highest. Ca was trapped in Ca-carbonate formation lowering the Ca released into the output solutions.

The increase of dioctahedral clay minerals with the pCO_2 increase (Figure 8.a) follows the trend of the final pH values leading to the highest Mg^{2+} released for the 1 pCO_2 experiment. Indeed, Mg^{2+} is a mobile cations in acidic conditions (Martini and Chesworth, 2013; Mason and Moore, 1982; Pedro and Delmas, 1970), which has also already been seen in natural conditions and is an important step for the mineralogical formation in weathering profiles similar to the martian one (Gaudin et al., 2011; Martini and Chesworth, 2013; Velde and Meunier, 2008). In addition, due to the higher formation of Al and Fe-rich clay minerals compared to the Fe,Mg-rich clay minerals during the water - 1 pCO_2 experiment, Mg^{2+} is less involved in the framework building of clay minerals, which let more Mg^{2+} in the solution (Gysi and Stefánsson, 2011). On the same initial material, Viennet et al. (2017) already showed the increase of dioctahedral bonds with the pCO_2 related to the pH decrease. The extents of dioctahedral layers were less important and carbonate formed because the experiments were performed in closed system setting. In closed system experiments, the continuous depletion of the alteration solution by the dissolution of the basaltic glass allows carbonate formation and lead to lesser dioctahedral clay minerals formation compared to the open system. Similar results have been obtained by Zolotov and Mironenko (2016) in their geochemical simulation devoted to the martian weathering profiles. Indeed in the simulation of 1 pCO_2 (Zolotov and Mironenko, 2016), the upper part of the soil is composed of Al-rich clay minerals and deeper, with the pH increase due to dissolution of the parent rock, $(Al,Fe)^{3+}$-rich clay minerals and carbonates are formed.

Except for the H_2SO_4 - 0.1 pCO_2 experiment, no oxides have been formed, thus the clay mineral formation explains the low release of Al and Fe into the output solution. Compared to Si, both Na and K have a high release, probably because they are not involved in the building of the framework minerals. Finally, the behavior of the chemical elements released controls the nature of the clay minerals formed.

4.2. Martian weathering profiles could have been formed under a dense CO_2 atmosphere

4.2.1. Experimental applicability

The experiments were performed at 150°C in order to decrease the reaction time. Indeed, with the increase of temperature, the dissolution rate of basaltic glass increases (Gislason and Oelkers, 2003; Gudbrandsson et al., 2011) leading to the reduction of the experiment duration. On Mars though, the weathering profiles were probably formed at much lower temperature. The temperature effect on the clay mineral evolution has already been described in geological systems. Observations for hydrothermal or diagenetic systems have shown that smectites, kaolinite or berthierine can be transformed into chlorites with increasing temperature (Beaufort et al. (2015) and references therein). The results obtained during the experiments show a non-negligible content of chlorites, which is probably higher than those of the martian weathering profiles (Noe Dobrea et al., 2010). Chlorites were over-formed, because of the hydrothermal/diagenetic chloritization process of smectite, kaolinite or berthierine (Beaufort et al., 2015; Meunier, 2005). In the review of Beaufort et al. (2015), three series of chloritization processes have been considered and described as Mg-series, Fe-series and Al,Mg-series. The Mg-series is identified by their $Fe/(Fe+Mg)_{octahedral} < 0.5$ while the Fe-series has ratios > 0.5. The Mg-series consists of the conversion of saponite to chlorite via corrensite. The Fe-series consists of the conversion of berthierine to chlorite to Fe-chlorite. And, the Al,Mg-series consists of the conversion of kaolinite to sudoite via tosudite. During the experiments presented here, the clay minerals formed are mainly composed of tri- and dioctahedral R0 smectite/chlorite and Fe-rich chlorite/smectite MLMs. The present experiments conducted at room temperature would probably have led to less chlorite formation in favor of smectite and kaolinite and to berthierine layers for the Fe-rich chlorite layers (Beaufort et al., 2015). Berthierine has not been identified in the weathering profiles but its presence cannot be excluding as its identification is close to Fe-rich smectite/chlorite MLM by NIR remote sensing (Calvin and King, 1997). Hence, the potential clay minerals formed at lower temperature are in line with the previous mineralogical description of the martian weathering profiles (Carter et al., 2015). The temperature effect modifies the relative proportion of chlorite, smectite, kaolinite or berthierine layers via mixed layering (Beaufort et al., 2015) but the octahedral compositions are partly influenced by the temperature (Beaufort et al., 2015; Cathelineau, 1988; Eberl et al., 1978; Inoue, 1983). Thus, the martian clay mineralogy, which is based on the octahedral composition investigated by NIR, can be compared to the NIR spectra of the experiment products by following the octahedral clay mineral composition evolution as presented in Figure 8.

The formation of the mineralogical assemblages is also dependent on the temperature. By performing experimental and modelling studies on basaltic glass of similar composition than the present study, Gysi and Stefánsson (2011, 2012a, 2012b) have shown that with the decrease of temperature the formation of carbonates is enhanced. Indeed, the formation of clay minerals is less important at lower temperature which let more Fe^{2+}, Mg^{2+} and Ca^{2+} be available for the carbonates formation. In a martian context, similar trend has been observed by geochemical modelling (Griffith and Shock, 1995) as with the temperature decrease, the formation of carbonates is promoted. Based on these studies, the content of carbonates formed can be enhanced up to ~15% between 150°C to 50°C. When applied to martian weathering profiles, our study minimized the content of carbonates formed. Also, the temperature effect (between 65 - 200°C) on the formation of sulfates in a martian context has been evaluated by Marcucci and Hynek, (2014). The type of sulfates formed is similar among the temperature tested but the amount of sulfates decreases with the temperature. Since no sulfate is formed during our experiments (Figures 3 and Table 3), no sulfate is expected to form at lower temperatures in the present experimental conditions either.

Summarizing the findings, the observed mineral assemblages produced at 150°C would evolve at lower temperature. Regarding the experiments involving CO_2, the carbonate content would increase (up to ~15%) with the temperature decrease and the content of clay minerals would decrease. No sulfate formed during the experiments involving H_2SO_4 fluids, and in colder conditions it is even less likely. Concerning the clay minerals, the temperature effect affects the relative proportions of the different species and mixed layering (Beaufort et al., 2015), as well as the octahedral compositions (Beaufort et al., 2015; Cathelineau, 1988; Eberl et al., 1978; Inoue, 1983). For the detailed comparison of the martian clay mineralogy the NIR spectra of the experiment products showing the octahedral clay mineral composition evolution as presented in Figure 8, can be used.

4.2.2. Martian clay mineral sequences better experimentally reproduced with CO_2-rich fluids

The widespread weathering profiles detected on the martian surface are composed of a sequence of dioctahedral clay minerals overlying di-trioctahedral clay minerals (Figure 9.a). The dioctahedral sequence is split in two from top with Al-rich clay minerals to bottom with an enrichment of Fe^{3+}-rich clay minerals (Carter et al., 2015; McKeown et al., 2009). The Figures 8 and 9.b show the experimental evolution of the octahedral composition of the clay minerals with the level # as a function of the pCO_2. As the experiments are performed from bottom to top, the level #1 corresponds to the top part of the stratigraphy while the levels #2 and #3 represent deeper soil horizons. In the present study, H_2SO_4 and HCl bearing solutions do not lead to significant dioctahedral clay mineral content (Figure 8.a and 9.b) nor to the evolution of Al to $(Al,Fe)^{3+}$-rich clay minerals (Figure 8.b) as observed on the martian weathering profiles (Figure 9). In addition, lower initial pH values lead to the formation of sulfates and inhibit smectite formation (Peretyazhko et al., 2018). Hence, the top layer of the martian weathering profiles is not experimentally reproduced by pure H_2SO_4 and HCl bearing solutions (Figure 9). The experiment able to form a top layer rich in dioctahedral clay minerals is the water - 1 pCO_2 (Figures 8.a and 9). In addition, this experiment is the only one suggesting horizons of Al-rich clay minerals above $(Al, Fe)^{3+}$-rich clay minerals (Figure 8.b). A CO_2-rich atmosphere is also in line with the alteration of olivine at low temperature under a dense CO_2 atmosphere (Gaudin et al., 2018). Indeed, a dense CO_2 atmosphere enables Al-rich clay mineral formation despite of an Al-poor parent rock. Drawing on the point of view of the clay mineralogy trend seen in the martian weathering profiles, we suggest that acidic alteration prompted by a dense CO_2-rich atmosphere better reproduce the martian weathering profiles (Figure 9). However, under a dense CO_2 atmosphere, carbonates are formed. The presence of carbonates in the weathering profiles is consistent with the thermal infrared spectra modelling predictions at Mawrth Vallis, which suggests up to 8% of carbonate (Bishop and

Rampe, 2016). Nevertheless, the mineral identification in the weathering profiles based on NIR measurements have not detected carbonates. Hence, Zolotov and Mironenko (2016) concluded that the weathering profiles were formed by low-pH H_2SO_4-bearing solutions rather than by S-free fluids (such as CO_2) and excluded the possibility of CO_2-rich fluids. Several previous studies argued that carbonate formation could have been inhibited despite of a dense CO_2 atmosphere by the addition of acidic solutions rich in sulfur. In the following, we discuss the geochemical consistency of proposed carbonate formation and of the carbonate detection limitation in light of our experimental results.

4.2.3. Are carbonates present in the martian weathering profiles?

Mineral detections challenged the geochemical interpretation of the weathering profile formation on Mars due to the lack of carbonate. Two main possibilities were proposed to explain the “missing” carbonates: i) a second acidic event, which led to carbonate dissolution (Bibring et al., 2006) or ii) a mixture of CO_2-rich and dense atmosphere with another gas leading to acidic solutions inhibiting the carbonate formation (Bullock and Moore, 2007; Fairén et al., 2004; Fernández-Remolar et al., 2011; Halevy et al., 2007). The first possibility suggests a second acidic event, driven by an acidic sulfuric fluid in equilibrium with a dense CO_2 atmosphere, dissolved any carbonates previously formed. However, such a secondary acidic event will dissolve carbonates, but carbonation would occur deeper in the profiles sequences as *in-situ* CO_2-storage experimentation have shown (Matter et al., 2016). In addition, the dissolution of carbonates could also lead to the release of CO_2 back into the atmosphere, cancelling the carbon sequestration, and thus not solving the “missing” carbonate paradox (Edwards and Ehlmann, 2015). The second possibility (Bullock and Moore, 2007; Fernández-Remolar et al., 2011; Halevy et al., 2007) aims to directly inhibit the carbonate formations during the alteration event. Acidic solutions rich in CO_2 mixed with other acids such as sulfuric acids were proposed to decrease the pH solutions lower than the pH range stability of carbonates. To test this possibility, the H_2SO_4 - 0.1 pCO_2 experiment was carried out. The results indicate that carbonates formed in the levels #2 and #3 and not in the level #1 (Figure 4). In contrast during the water - 0.1 pCO_2 experiment, carbonates were formed in all three levels. These results are supported by geochemical simulations. Xu et al. (2007) have shown that the quantities of carbonates formed are the same, independently of any presence of SO_2, but the carbonate precipitation is found deeper in the profiles with the addition of sulfur fluid alteration. The numerically simulated martian weathering profiles (Zolotov and Mironenko, 2016) show that H_2SO_4-solution with a low-pCO_2 dissolved led to carbonates in the middle part of weathering profiles when the pH solution rises up neutral values. Lastly, even if a sulfuric-rich solution mixed with CO_2 has ever existed on early Mars, the acidic consumption due to the parent rock dissolution along the hundreds of meters depth of the weathering profiles (i.e. such as Mawrth Vallis, Carter et al. (2015)) would have led to carbonation. Hence, the detections of carbonates in the middle section of the weathering profiles (Bultel et al., 2019) are in agreement with the above results.

A confident identification of carbonates is difficult when they are mixed with clay minerals and/or present in small amounts (this study, Sutter et al., 2007). Figure 10 displays examples of NIR spectra of hydrothermal carbonates detected on the Martian surface (Viviano et al. 2014), in the martian weathering profiles (Bultel et al., 2019) and our spectrum of experimentally produced carbonate mixed with clay minerals obtained during in the level #1 of the water - 0.1 pCO_2 experiment (Figure 10.c). The qualitative carbonate identification on Mars with the Compact Reconnaissance Imaging Spectrometer for Mars (CRISM) in the NIR range is based on the combination band near 2.30, 2.50, 3.50 and 3.85 µm (Figure 10) (i.e. Bultel et al., (2019)). No 2.3 and 2.5 µm adsorption band of carbonate are present in our experimental spectra nor in the spectra of the observed weathering profiles on Mars. In the CRISM NIR range, without the 3.95 µm band and the carbonate XRD peaks for the experiments, it would be impossible to attribute the weak 3.85 µm bands to carbonates. Hence, the detection of carbonates in the martian weathering profiles is challenging. Nevertheless, as discussed in the section 4.2.1, the content of carbonate should increase by 15% if the experiments would have been carried out at lower temperature (i.e. <50°C). In such conditions, the detections of carbonates from orbit could perhaps be possible as shown by Bultel et al., (2019). Indeed, on Mars, the only place where carbonates have been detecting by both orbital instrument and in-situ analysis is at Gusev crater (Morris et al., 2010; Carter and Poulet, 2012). The origin of carbonates is hydrothermal, and the carbonate content measured *in-situ* was between 16-34 weight % (Morris et al., 2010). Such content of carbonate allows their detection from the orbit. As shown here, more carbonates could be detected on the martian surface but it would be challenging due to the potential low carbonate proportions, the mixture of carbonates with clay minerals, the low spatial resolution of the orbital instruments, and the low signal to noise ratio at > 3.5 µm wavelengths (Murchie et al, 2007).

Our study is a first attempt to reproduce the entire stratigraphy by experimental work. The present results cannot explain all observations made in the weathering profiles. Several more parameters can be tested to better decipher the martian environment when the weathering profiles formed. The temperature effect on the mineral formation has to be more documented experimentally. Also, the present study does not explain the local presence of sulfates at Marwth Vallis, which would require additional information of whether they formed simultaneously or subsequently. Testing more various mixtures between H_2SO_4 acid and CO_2 gas will adds constraints to the formation competition between sulfates, carbonates and clay minerals. This would help to determine if it is possible to form sulfates during the weathering profile formation or rather subsequently during the Hesperian when Mars has become a sulfuric rich environment. Finally, such investigations would provide more information on the chemical composition of acidic fluids and hence would better determine the atmospheric composition during the weathering profile formation.

5. Conclusion and remarks

In the present study, an open column experimental system is used to mimic martian weathering of the Noachian. We tested different input solution in equilibrium with various pCO_2 (water - 1 pCO_2, water - 0.1 pCO_2, HCl - 0 pCO_2, H_2SO_4 - 0 pCO_2 and H_2SO_4 - 0.1 pCO_2) to investigate the composition of early martian atmosphere. The results obtained show that the output pH values decrease with the increase of pCO_2 leading to an enhanced dioctahedral clay mineral formation when CO_2 is present. In addition, the Al-rich to $(Al,Fe)^{3+}$-rich clay mineral zone observed in the martian weathering profiles are better reproduce during the water - 1 pCO_2 experiment. Comparing the experimentally produced and remotely observed clay mineral sequences, the top part of the weathering profiles is better reproduced by acidic solution under a dense CO_2

atmosphere. With such CO_2-rich fluids, carbonates form. Despite previous studies explaining the absence of carbonates by the role of acidic fluids, we suggest that carbonates should be present in the weathering sequences even if additional acidic solutions were present. It could explain the recent detections of carbonates in the middle part of the weathering profiles. We propose that the identification of carbonates using the NIR CRISM instrument is challenged by their low abundance, the presence of clay minerals and the orbital instruments limitations, such as the wavelength range and the spatial/spectral resolutions. Finally, we suggest that the predominance of dioctahedral-rich clay minerals and their evolution in the top horizons, are in better agreement with an acidic weathering under a dense CO_2 atmosphere. In such conditions, carbonates are formed in the middle part of the weathering profiles as observed by Bultel et al., (2019). Such atmosphere is in line with the climatic studies (Wordsworth, 2016) investigating the liquid water stability on the martian surface. Nevertheless, further experimental work and observation of the surface mineral composition of Mars (in situ or remote sensing) are needed to better constrain the early martian environment and atmosphere. The contribution of various pCO_2 and H_2SO_4 (or other acids, gasses) concentrations in future experiments will allow for additional constraints on the boehmite, sulfate and carbonate precipitations and their positions with respect to the clay mineralogy of the weathering sequence. The influence of temperature has to be evaluated to highlight the evolution of the mineralogical assemblages. Finally, mineralogical association and formation competition (Viennet et al., 2017 and this study) are a promising proxy to decipher the early martian fluid compositions and consequently the early atmospheric compositions and conditions as well.

Figure captions

Figure 1: Schema of the open-column system used for performing the experiments. The input fluid is in equilibrium with the gas reservoir. Then this solution is injected into the titanium cylinder using a high pressure liquid chromatography (HPLC) pump. The fluid passes through the three shelves containing basaltic powder. Finally the output solution passes through a backpressure regulator (BPR) and is collected in a container. The pressure inside the system is controlled by the BPR and measured a pressure gauge. To decrease the time of reaction, the temperature was set at 150°C and the fluid was kept liquid by setting the pressure to 5 bars.

Figure 2: (a-e) the solid lines with symbols correspond to the measured pH at 25°C of the output solution as a function of time. The solid lines correspond to the initial pH at 25°C. The symbols correspond to the consumption of H^+ in $mol.L^{-1}$ as a function of time: $[H^+]_{consumption} = [H^+]_{initial} - [H^+]_{final}$. (f-j) The solid lines correspond to the initial pH calculated at 150°C. The pH values at 150°C are calculated from the chemical concentrations of the major chemical elements and the pH measurements of the output solution (filled symbols on the right).

Figure 3: (a-e) total quantities of elements released in mol in the output solutions as a function of time. The quantities of Al and Fe are considered negligible because their concentrations are two orders of magnitude lower than Si and are not shown. (f) Mg/Si, (g) Ca/Si, (h) Na/Si and (i) K/Si ratios of the elements measured in the output solutions as a function of time. The black solid line corresponds to the ratios of the unreacted samples (Table 1).

Figure 4: Bulk XRD patterns and NIR spectra of the unreacted basalt. The XRD measurement shows that the main content is a basaltic glass with olivine, pyroxene (forsterite and augite, respectively, see EDS measurements Figure S1) and quartz. The NIR measurement highlights the presence of forsterite and augite.

Figure 5: Comparison of the bulk XRD patterns of the reacted basaltic glass as a function of the level # and the experimental conditions.

Figure 6: Comparison of the NIR spectra of the reacted basaltic glass as a function of the level # and the experimental conditions.

Figure 7: Comparison of the NIR spectra with continuum removed for the range between 2.1 and 2.5 µm as a function of the level # and experimental conditions. The adsorption bands related to the Al_2- and $(Al,Fe)_2$-OH bonds (at 2.19 and 2.25 µm) decrease with the pCO_2 and the increase of level # in favor of the $(Fe,Mg)_3$-OH bonds (at 2.31 and 2.35 µm).

Figure 8: Evolution of the octahedral composition of the clay minerals formed as a function of the pCO_2 and level #. **a.** Evolution of the di-/trioctahedral character of the clay minerals formed as a function of pCO_2 and acid used. (Al_2 + $(Al,Fe)_2/(Fe,Mg)_2$) absorption band depths correspond to the ratio of the absorption band related to dioctahedral clay minerals (sum of the 2.20 and 2.25 µm absorption bands depths) and trioctahedral clay minerals (sum of the 2.31 and 2.35 µm bands depths). The results show that with the increase of pCO_2, the clay minerals formed are more dioctahedral. **b.** Evolution of the Al_2 and $(Al,Fe)_2$ character of the clay minerals formed as a function of pCO_2 and acid used. The Al_2 /(Al_2 + $(Al,Fe)_2$) corresponds to the absorption band depth of the Al_2-OH band at 2.20 µm. $(Al,Fe)_3$ corresponds to the absorption band depth of the $(Al,Fe)_2$-OH band at 2.31 µm. A transition from Al_2 rich to Al,Fe rich clay minerals is only produced during the water - 1 pCO_2 experiment. The grey bar, representing the noise level, corresponds to the level at which a low adsorption due to metal-OH bonds and noise cannot be differentiate. In such case, the adsorption is considered null.

Figure 9: Sketch of the mineral detection for the martian weathering profiles (a.) compared to the experimental results for each level# placed in the stratigraphy based on the di-trioctahedral ratio (see Figure 8.a). Based on this comparison, the weathering profiles are better reproduced by using a pCO_2 of 1.

Figure 10: NIR spectra comparing carbonates detections on Mars from the orbit of hydrothermal carbonates (Viviano-Beck et al., 2014), carbonates in weathering profiles (Bultel et al., 2019) and one experimental residue (level #1 of the water – 0.1 pCO_2 experiment) where the presence of carbonate have been confirmed by XRD measurements. The comparison shows the difficulty to detect carbonate in the martian weathering profiles.

Tables

Table 1: Total chemistry in oxides of the original basalt used in the present study.

Oxides	SiO_2	Al_2O_3	FeO(T)	MgO	Na_2O	K_2O	CaO	TiO2	Minor elements*	Total
%	48.2	14.2	10.8	9.4	1.9	0.3	11.7	1.6	1.9	100

* SO3, Cr2O3, MnO, Co3O4, NiO, CuO, ZnO, SeO2, SrO, I, Au.

Table 2: Initial experimental conditions showing the fluid and gas composition and their related initial pH.

Experiment	Gas composition at 1 bar and 20°C	Fluid composition	pH initial (20°C)/(150°C)
water – 1 pCO_2	100 % CO_2	Pure water	3.90 / 4.10
water – 0.1 pCO_2	90 % CO_2 / 10 % N_2	Pure water	4.40 / 4.60
H_2SO_4 – 0 pCO_2	100 % N_2	H_2SO_4 at pH3	3.00 / 3.20
HCl – 0 pCO_2	100 % N_2	HCl at pH3	3.00 / 3.50
H_2SO_4 – 0.1 pCO_2	90 % CO_2 / 10 % N_2	H_2SO_4 at pH3	2.98 / 3.17

Table 3: Overview of the minerals formed as a function of the experiments conditions and level #. The symbols -, +, ++, +++ represents the relative abundance of minerals estimated from XRD and NIR measurements. *boehmite is not reported in the table because it has been formed only for the H_2SO_4 - 0.1 pCO_2 experiments in the level # 1.

		Dissolution %			Dioctahedral chlorite/smectite			Trioctahedral smectite/chlorite			Carbonates		
Experiments	pH final (20°C/150°C)	Level			Level			Level			Level		
		#1	#2	#3	#1	#2	#3	#1	#2	#3	#1	#2	#3
water – 1 pCO_2	6.35 / 6.07	75	60	45	+++	+++	++	+	+	++	-	-	+
water – 0.1 pCO_2	8.08 / 7.01	60	55	40	++	++	+	+	++	++	+	++	++
H_2SO_4 – 0 pCO_2	8.59 / 7.04	55	40	30	+	-	-	++	+++	+++	-	-	-
HCl – 0 pCO_2	8.53 / 7.02	55	40	30	+	-	-	++	+++	+++	-	-	-
H_2SO_4 – 0.1 pCO_2^*	8.32 / 6.88	60	50	40	++	-	-	++	+++	+++	-	+	+

Acknowledgments

This work was partly supported by the Research Council of Norway through its Centre of Excellence funding scheme, project 223272. This project has received funding from the European Union's Horizon 2020 (H2020-COMPET-2015) Research and Innovation Program under grant agreement 687302 (PTAL). This study is supported by the Research Council of Norway (235058/F20 CRATER CLOCK). The authors would like to thank B. Foroughinejad (Chemistry, University of Oslo) for technical support setting up the experiments, F Poulet and L. Riu (IAS-University Paris-Sud) for access and help during the NIR measurements, and H. Hellevang and H. Dypvik (Geosciences, University of Oslo) for providing the sample. We would like to greatly thank the Plateau Technique de Microscopie Electronique (Museum National d'Histoire Naturelle, Paris) for the SEM pictures and the EDS analyses. A special thanks goes to S. Pont for performing the SEM and EDS analysis. The authors wish to acknowledge the editor in chief Dr. Michael E. Böttcher and the three anonymous reviewers for their constructive comments that greatly improved the quality of this work.

References

Adams J. B. (1974) Visible and near-infrared diffuse reflectance spectra of pyroxenes as applied to remote sensing of solid objects in the solar system. J. Geophys. Res. 79, 4829–4836.

Beaufort, D., Rigault, C., Billon, S., Billault, V., Inoue, A., Inoue, S. and Patrier, P. (2015) Chlorite and chloritization processes through mixed-layer mineral series in low-temperature geological systems – a review. Clay Minerals 50, 497-523.

Bell J., (2008) The Martian Surface-Composition, Mineralogy, and Physical Properties. Cambridge Planetary Science.

Bibring, J.-P., Hamm, V., Pilorget, C. and Vago, J.L. (2017) The MicrOmega Investigation Onboard ExoMars. Astrobiology 17, 621-626.

Bibring, J.P., Langevin, Y., Mustard, J.F., Poulet, F., Arvidson, R., Gendrin, A., Gondet, B., Mangold, N., Pinet, P., Forget, F., Berthe, M., Bibring, J.P., Gendrin, A., Gomez, C., Gondet, B., Jouglet, D., Poulet, F., Soufflot, A., Vincendon, M., Combes, M., Drossart, P., Encrenaz, T., Fouchet, T., Merchiorri, R., Belluci, G., Altieri, F., Formisano, V., Capaccioni, F., Cerroni, P., Coradini, A., Fonti, S., Korablev, O., Kottsov, V., Ignatiev, N., Moroz, V., Titov, D., Zasova, L., Loiseau, D., Mangold, N., Pinet, P., Doute, S., Schmitt, B., Sotin, C., Hauber, E., Hoffmann, H., Jaumann, R., Keller, U., Arvidson, R., Mustard, J.F., Duxbury, T., Forget, F. and Neukum, G. (2006) Global mineralogical and aqueous mars history derived from OMEGA/Mars Express data. Science (New York, N.Y.) 312, 400-404.

Bish D. L., Blake D. F., Vaniman D. T., Chipera S. J., Morris R. V, Ming D. W., Treiman A. H., Sarrazin P., Morrison S. M., Downs R. T., Achilles C. N., Yen A. S., Bristow T. F., Crisp J. A., Morookian J. M., Farmer J. D., Rampe E. B., Stolper E. M. and Spanovich N. (2013) X-ray Diffraction Results from Mars Science Laboratory: Mineralogy of Rocknest at Gale Crater. Science (80-.). 341, 1238932.

Bishop, J.L. and Rampe, E.B. (2016) Evidence for a changing Martian climate from the mineralogy at Mawrth Vallis. Earth and Planetary Science Letters 448, 42-48.

Bishop J. L., Loizeau D., McKeown N. K., Saper L., Dyar M. D., Des Marais D. J., Parente M. and Murchie S. L. (2013) What the ancient phyllosilicates at Mawrth Vallis can tell us about possible habitability on early Mars. Planet. Space Sci. 86, 130–149.

Bishop J. L., Pieters C. M. and Edwards J. O. (1994) Infrared spectroscopic analyses on the nature of water in montmorillonite. Clays Clay Miner. 42, 702–716.

Bullock, M.A. and Moore, J.M. (2007) Atmospheric conditions on early Mars and the missing layered carbonates. Geophysical Research Letters 34.

Bultel B., Viennet J.-C., Poulet F., Carter J. and Werner, S. C. (2019) Detection of carbonates in Martian weathering profiles. Journal of Geophysical Research: Planets, 124, 989–1007.

Calvin, W. M. and King, T. V. (1997) Spectral characteristics of iron-bearing phyllosilicates: Comparison to Orgueil (CI1), Murchison and Murray (CM2). *Meteoritics & Planetary Science*, *32*(5), 693-701.

Carter, J., Loizeau, D., Mangold, N., Poulet, F. and Bibring, J.-P. (2015) Widespread surface weathering on early Mars: A case for a warmer and wetter climate. Icarus 248, 373-382.

Carter J. and Poulet F. (2012) Orbital identification of clays and carbonates in Gusev crater. Icarus 219, 250–253.

Cathelineau, M. (1988) Cation site occupancy in chlorites and illites as function of temperature. Clay minerals 23, 471-485.

Chipera S. J. and Bish D. L. (2013) Fitting full X-ray diffraction patterns for quantitative analysis: a method for readily quantifying crystalline and disordered phases. Adv. Mater. Phys. Chem. 3, 47.

Clark R. N., Gallagher A. J. and Swayze G. A. (1990) Material absorption band depth mapping of imaging spectrometer data using a complete band shape least-squares fit with library reference spectra. In Proceedings of the Second Airborne Visible/Infrared Imaging Spectrometer (AVIRIS) Workshop JPL Publication 90-54. pp. 176–186.

Cloutis E., Goltz D., Coombs J., Attas M., Majzels C. and Collins C. (2003) Non-destructive discrimination of artists' white materials using bidirectional reflectance spectroscopy. Canadian Journal of Analytical Sciences and Spectroscopy 48, 157-170.

Cloutis E. A., Gaffey M. J., Jackowski T. L. and Reed K. L. (1986) Calibrations of phase abundance, composition, and particle size distribution for olivine-orthopyroxene mixtures from reflectance spectra. J. Geophys. Res. Solid Earth 91, 11641–11653.

Craddock, R.A. and Greeley, R. (2009) Minimum estimates of the amount and timing of gases released into the martian atmosphere from volcanic eruptions. Icarus 204, 512-526.

Dehouck E., Gaudin A., Mangold N., Lajaunie L., Dauzères A., Grauby O. and Le Menn E. (2014a) Weathering of olivine under CO2 atmosphere: A martian perspective. Geochim. Cosmochim. Acta 135, 170–189.

Dehouck E., McLennan S. M., Meslin P.-Y. and Cousin A. (2014b) Constraints on abundance, composition, and nature of X-ray amorphous components of soils and rocks at Gale crater, Mars. J. Geophys. Res. Planets 119, 2640–2657.

Eberl, D., Whitney, G. and Khoury, H. (1978) Hydrothermal reactivity of smectite. American Mineralogist 63, 401-409.

Edwards, C.S. and Ehlmann, B.L. (2015) Carbon sequestration on Mars. Geology 43, 863-866.

Farrand W. H., Glotch T. D. and Horgan B. (2014) Detection of copiapite in the northern Mawrth Vallis region of Mars: Evidence of acid sulfate alteration, Icarus 241, 346–357.

Farrand W. H., Glotch T. D., Rice J. W., Hurowitz J. A. and Swayze G. A. (2009) Discovery of jarosite within the Mawrth Vallis region of Mars: Implications for the geologic history of the region. Icarus 204, 478–488.

Fairén, A.G., Fernández-Remolar, D., Dohm, J.M., Baker, V.R. and Amils, R. (2004) Inhibition of carbonate synthesis in acidic oceans on early Mars. Nature 431, 423-426.

Fernández-Remolar, D.C., Sánchez-Román, M., Hill, A.C., GÓMez-OrtÍZ, D., Ballesteros, O.P., Romanek, C.S. and Amils, R. (2011) The environment of early Mars and the missing carbonates. Meteoritics & Planetary Science 46, 1447-1469.

Forget, F., Wordsworth, R., Millour, E., Madeleine, J.-B., Kerber, L., Leconte, J., Marcq, E. and Haberle, R.M. (2013) 3D modelling of the early martian climate under a denser CO 2 atmosphere: Temperatures and CO2 ice clouds. Icarus 222, 81-99.

Gaudin A., Dehouck E., Grauby O. and Mangold N. (2018) Formation of clay minerals on Mars: Insights from long-term experimental weathering of olivine. Icarus 311, 210–223.

Gaudin, A., Dehouck, E. and Mangold, N. (2011) Evidence for weathering on early Mars from a comparison with terrestrial weathering profiles. Icarus 216, 257-268.

Gislason S. R. and Oelkers E. H. (2003) Mechanism, rates, and consequences of basaltic glass dissolution: II. An experimental study of the dissolution rates of basaltic glass as a function of pH and temperature. Geochim. Cosmochim. Acta 67, 3817–3832.

Gislason S. R., Arnorsson S. and Armannsson H. (1996) Chemical weathering of basalt in Southwest Iceland; effects of runoff, age of rocks and vegetative/glacial cover. Am. J. Sci. 296, 837–907.

Gislason S. R. and Arnórsson S. (1993) Dissolution of primary basaltic minerals in natural waters: saturation state and kinetics. *Chem. Geol.* **105**, 117–135.

Gislason S. R. and Hans P. E. (1987) Meteoric water-basalt interactions. I: A laboratory study. *Geochim. Cosmochim. Acta* **51**, 2827–2840.

Griffith L. L. and Shock E. L. (1995) A geochemical model for the formation of hydrothermal carbonates on Mars. Nature 377, 406–408.

Gudbrandsson S., Wolff-Boenisch D., Gislason S. R. and Oelkers E. H. (2011) An experimental study of crystalline basalt dissolution from $2 \leqslant pH \leqslant 11$ and temperatures from 5 to 75 °C. Geochim. Cosmochim. Acta 75, 5496–5509.

Gysi A. P. and Stefánsson A. (2012a) CO2-water–basalt interaction. Low temperature experiments and implications for CO2 sequestration into basalts. *Geochim. Cosmochim. Acta* **81**, 129–152.

Gysi A. P. and Stefánsson A. (2012b) Experiments and geochemical modeling of CO2 sequestration during hydrothermal basalt alteration. Chem. Geol. 306–307, 10–28.

Gysi, A.P. and Stefánsson, A. (2011) CO2–water–basalt interaction. Numerical simulation of low temperature CO2 sequestration into basalts. Geochim. Cosmochim. Acta 75, 4728-4751.

Halevy, I. and Iii, J.W.H. (2014) Episodic warming of early Mars by punctuated volcanism. Nature Geoscience 7, 865.

Halevy, I., Zuber, M.T. and Schrag, D.P. (2007) A sulfur dioxide climate feedback on early Mars. Science (New York, N.Y.) 318, 1903-1907.

Hunt G. R. (1977) Spectral signatures of particulate minerals in the visible and near infrared. Geophysics 42, 501–513.

Hunt G. R. and Salisbury J. W. (1971) Visible and near infrared spectra of minerals and rocks. II. Carbonates. Mod. Geol. 2, 23–30

Inoue, A. (1983) Potassium fixation by clay minerals during hydrothermal treatment. Clays and Clay Minerals 31, 81-91.

Kerber, L., Forget, F. and Wordsworth, R. (2015) Sulfur in the early martian atmosphere revisited: Experiments with a 3-D Global Climate Model. Icarus 261, 133-148.

King T. V. V and Clark R. N. (1989) Spectral characteristics of chlorites and Mg-serpentines using high-resolution reflectance spectroscopy. J. Geophys. Res. Solid Earth 94, 13997–14008

Lammer, H., Chassefière, E., Karatekin, Ö., Morschhauser, A., Niles, P.B., Mousis, O., Odert, P., Möstl, U.V., Breuer, D. and Dehant, V. (2013) Outgassing history and escape of the martian atmosphere and water inventory. Space Science Reviews 174, 113-154.

Marcucci E. C. and Hynek B. M. (2014) Laboratory simulations of acid-sulfate weathering under volcanic hydrothermal conditions: Implications for early Mars. J. Geophys. Res. Planets 119, 679–703.

Martini, I.P. and Chesworth, W. (2013) Weathering, soils & paleosols. Elsevier.

Mason, B. and Moore, C.B. (1982) Principles of Geochemistry, 4th edition ed. John Wiley and soons, New York.

Matter, J.M., Stute, M., Snæbjörnsdottir, S.Ó., Oelkers, E.H., Gislason, S.R., Aradottir, E.S., Sigfusson, B., Gunnarsson, I., Sigurdardottir, H., Gunnlaugsson, E., Axelsson, G., Alfredsson, H.A., Wolff-Boenisch, D., Mesfin, K., Taya, D.F.d.l.R., Hall, J., Dideriksen, K. and Broecker, W.S. (2016) Rapid carbon mineralization for permanent disposal of anthropogenic carbon dioxide emissions. Science (New York, N.Y.) 352, 1312-1314.

McKeown, N.K., Bishop, J.L., Noe Dobrea, E.Z., Ehlmann, B.L., Parente, M., Mustard, J.F., Murchie, S.L., Swayze, G.A., Bibring, J.P. and Silver, E.A. (2009) Characterization of phyllosilicates observed in the central Mawrth Vallis region, Mars, their potential formational processes, and implications for past climate. Journal of Geophysical Research: Planets 114.

McSween H. Y., Wyatt M. B., Gellert R., Bell III J. F., Morris R. Van, Herkenhoff K. E., Crumpler L. S., Milam K. A., Stockstill K. R. and Tornabene L. L. (2006) Characterization and petrologic interpretation of olivine-rich basalts at Gusev Crater, Mars. J. Geophys. Res. Planets 111.

Melwani Daswani, M. and Kite, E.S. (2017) Paleohydrology on Mars constrained by mass balance and mineralogy of pre-Amazonian sodium chloride lakes. Journal of Geophysical Research: Planets 122, 1802-1823.

Meslin P.-Y., Gasnault O., Forni O., Schröder S., Cousin A., Berger G., Clegg S. M., Lasue J., Maurice S., Sautter V., Le Mouélic S., Wiens R. C., Fabre C., Goetz W., Bish D., Mangold N., Ehlmann B., Lanza N., Harri A.-M., Anderson R., Rampe E., McConnochie T. H., Pinet P., Blaney D., Léveillé R., Archer D., Barraclough B., Bender S., Blake D., Blank J. G., Bridges N., Clark B. C., DeFlores L., Delapp D., Dromart G., Dyar M. D., Fisk M., Gondet B., Grotzinger J., Herkenhoff K., Johnson J., Lacour J.-L., Langevin Y., Leshin L., Lewin E., Madsen M. B., Melikechi N., Mezzacappa A., Mischna M. A., Moores J. E., Newsom H., Ollila A., Perez R., Renno N., Sirven J.-B., Tokar R., de la Torre M., d'Uston L., Vaniman D. and Yingst A. (2013) Soil Diversity and Hydration as Observed by ChemCam at Gale Crater, Mars. Science (80-.). 341, 1238670.

Meunier, A. (2005) Clays. Springer Science & Business Media.

Michalski, J.R., Niles, P., Cuadros, J. and Baldridge, A. (2013) Multiple working hypotheses for the formation of compositional stratigraphy on Mars: Insights from the Mawrth Vallis region. Icarus 226, 816-840.

Morris R. V, Ruff S. W., Gellert R., Ming D. W., Arvidson R. E., Clark B. C., Golden D. C., Siebach K., Klingelhöfer G. and Schröder C. (2010) Identification of carbonate-rich outcrops on Mars by the Spirit rover. Science (80-.)., 1189667.

Murchie S., Arvidson R., Bedini P., Beisser K., Bibring J.-P., Bishop J., Boldt J., Cavender P., Choo T., Clancy R. T., Darlington E. H., Des Marais D., Espiritu R., Fort D., Green R., Guinness E., Hayes J., Hash C., Heffernan K., Hemmler J., Heyler G., Humm D., Hutcheson J., Izenberg N., Lee R., Lees J., Lohr D., Malaret E., Martin T., McGovern J. A., McGuire P., Morris R., Mustard J., Pelkey S., Rhodes E., Robinson M., Roush T., Schaefer E., Seagrave G., Seelos F., Silverglate P., Slavney S., Smith M., Shyong W.-J., Strohbehn K., Taylor H., Thompson P., Tossman B., Wirzburger M. and Wolff M. (2007) Compact Reconnaissance Imaging Spectrometer for Mars (CRISM) on Mars Reconnaissance Orbiter (MRO). J. Geophys. Res. Planets 112.

Noe Dobrea, E., Bishop, J., McKeown, N., Fu, R., Rossi, C., Michalski, J., Heinlein, C., Hanus, V., Poulet, F. and Mustard, R. (2010) Mineralogy and stratigraphy of phyllosilicate-bearing and dark mantling units in the greater Mawrth Vallis/west Arabia Terra area: Constraints on geological origin. Journal of Geophysical Research: Planets 115.

Oelkers, E.H. and Gislason, S.R. (2001) The mechanism, rates and consequences of basaltic glass dissolution: I. An experimental study of the dissolution rates of basaltic glass as a function of aqueous Al, Si and oxalic acid concentration at 25°C and pH = 3 and 11. Geochim. Cosmochim. Acta 65, 3671-3681.

Osterloo, M.M., Anderson, F.S., Hamilton, V.E. and Hynek, B.M. (2010) Geologic context of proposed chloride-bearing materials on Mars. Journal of Geophysical Research: Planets 115.

Pedro, G. and Delmas, A. (1970) Geo-chemical principles of the distribution of trace elements in soils, Annales Agronomiques, pp. 483-518.

Peretyazhko, T.S., Niles, P.B., Sutter, B., Morris, R.V., Agresti, D.G., Le, L. and Ming, D.W. (2018) Smectite formation in the presence of sulfuric acid: Implications for acidic smectite formation on early Mars. Geochim. Cosmochim. Acta 220, 248-260.

Ramirez, R.M. (2017) A warmer and wetter solution for early Mars and the challenges with transient warming. Icarus 297, 71-82.

Rull, F., Maurice, S., Hutchinson, I., Moral, A., Perez, C., Diaz, C., Colombo, M., Belenguer, T., Lopez-Reyes, G. and Sansano, A. (2017) The Raman Laser Spectrometer for the ExoMars Rover Mission to Mars. Astrobiology 17, 627-654.

Skougstad, M.W., Fishman, M., Friedman, L., Erdmann, D. and Duncan, S. (1978) Methods for analysis of inorganic substances in water and fluvial sediments.

Smith R. J., Rampe E. B., Horgan B. H. N. and Dehouck E. (2018) Deriving Amorphous Component Abundance and Composition of Rocks and Sediments on Earth and Mars. J. Geophys. Res. Planets 123, 2485–2505.

Stefánsson A., Gíslason S. R. and Arnórsson S. (2001) Dissolution of primary minerals in natural waters: II. Mineral saturation state. *Chem. Geol.* **172**, 251–276.Strachan, D. (2017) Glass dissolution as a function of pH and its implications for understanding mechanisms and future experiments 219, 111-123.

Sutter, B., Dalton, J. B., Ewing, S. A., Amundson, R. and McKay C. P. (2007) Terrestrial analogs for interpretation of infrared spectra from the Martian surface and subsurface: Sulfate, nitrate, carbonate, and phyllosilicate-bearing Atacama Desert soils. Journal of Geophysical Research: Biogeosciences, 112, G04S10.

Velde, B.B. and Meunier, A. (2008) The origin of clay minerals in soils and weathered rocks. Springer Science & Business Media.

Viennet, J.-C., Bultel, B., Riu, L. and Werner, S.C. (2017) Dioctahedral phyllosilicates versus zeolites and carbonates versus zeolites competitions as constraints to understanding early Mars alteration conditions. Journal of Geophysical Research: Planets 122, 11, 2328-2343.

Viviano-Beck, C.E., Seelos, F.P., Murchie, S.L., Kahn, E.G., Seelos, K.D., Taylor, H.W., Taylor, K., Ehlmann, B.L., Wiseman, S.M. and Mustard, J.F. (2014) Revised CRISM spectral parameters and summary products based on the currently detected mineral diversity on Mars. Journal of Geophysical Research: Planets 119, 1403-1431.

Wolery, T.J. (1992) EQ3/6, A Software Package for Geochemical Modeling of Aqueous Systems: Package Overview and Installation Guide (Version 7.0): UCRL-MA-110662-PT-I. Lawrence Livermore National Laboratory, Livermore, California. .

Wordsworth, R., Kalugina, Y., Lokshtanov, S., Vigasin, A., Ehlmann, B., Head, J., Sanders, C. and Wang, H. (2017) Transient reducing greenhouse warming on early Mars. Geophysical Research Letters 44, 665-671.

Wordsworth, R.D. (2016) The climate of early Mars. Annual Review of Earth and Planetary Sciences 44, 381-408.

Xu, T., Apps, J.A., Pruess, K. and Yamamoto, H. (2007) Numerical modeling of injection and mineral trapping of CO 2 with H 2 S and SO 2 in a sandstone formation. Chemical Geology 242, 319-346.

Zolotov, M. Yu., and Mironenko, M. V. (2007) Timing of acid weathering on Mars: A kinetic-thermodynamic assessment. Journal of Geophysical Research [Planets] 112, E07006.

Zolotov, M.Y. and Mironenko, M.V. (2016) Chemical models for martian weathering profiles: Insights into formation of layered phyllosilicate and sulfate deposits. Icarus 275, 203-220.

Supporting information for

Experimental reproduction of the martian weathering profiles argues for a dense Noachian CO_2 atmosphere

Jean-Christophe Viennet[a]*, Benjamin Bultel[a], Stephanie C. Werner[a]

[a] Centre for Earth Evolution and Dynamics, Department for Geosciences, University of Oslo, Postboks 1028 Blindern, 0316 Oslo, Norway

* Now at Muséum National d'Histoire Naturelle, Institut de Minéralogie, Physique des Matériaux et Cosmochimie, CNRS UMR 7590, Sorbonne Université, CNRS, F-75005 Paris, France.* Author to whom correspondence should be addressed:

Jean-Christophe Viennet

Email address: jean.christophe.viennet25@gmail.com

Centre for Earth Evolution and Dynamics, Department for Geosciences, University of Oslo, Postboks 1028 Blindern, 0316 Oslo, Norway

Table S1: Total quantities of elements released in mol in the output solutions as a function of time and of the experiments.

Water - 1 pCO2							
T (H)	Si (mol)	Al (mol)	Fe (mol)	Na (mol)	K (mol)	Mg (mol)	Ca (mol)
69	1.59E-03	2.58E-06	0.00E+00	1.50E-04	3.00E-05	1.94E-04	2.00E-04
122	2.70E-03	5.96E-06	0.00E+00	2.43E-04	4.23E-05	3.34E-04	3.77E-04
166	3.53E-03	9.99E-06	0.00E+00	3.18E-04	5.00E-05	4.08E-04	6.12E-04
214	4.50E-03	1.51E-05	0.00E+00	3.95E-04	6.80E-05	4.87E-04	8.71E-04
262	5.53E-03	2.01E-05	0.00E+00	4.74E-04	7.81E-05	5.66E-04	1.13E-03
310	6.59E-03	2.52E-05	0.00E+00	5.43E-04	9.52E-05	6.61E-04	1.40E-03
358	7.81E-03	2.98E-05	0.00E+00	6.09E-04	1.06E-04	7.78E-04	1.60E-03
431	9.59E-03	3.46E-05	5.38E-08	7.02E-04	1.36E-04	9.57E-04	2.03E-03

Water - 0.1 pCO2							
T (H)	Si (mol)	Al (mol)	Fe (mol)	Na (mol)	K (mol)	Mg (mol)	Ca (mol)
42	4.95E-04	2.57E-06	0.00E+00	8.48E-05	2.54E-05	0.00E+00	6.35E-05
90	1.17E-03	7.04E-06	0.00E+00	1.57E-04	5.30E-05	0.00E+00	1.48E-04
137	1.79E-03	1.20E-05	0.00E+00	2.17E-04	7.32E-05	0.00E+00	2.32E-04
210	2.73E-03	2.05E-05	0.00E+00	3.09E-04	9.57E-05	0.00E+00	3.67E-04
260	3.34E-03	2.66E-05	0.00E+00	3.66E-04	1.06E-04	0.00E+00	4.59E-04
431	5.51E-03	4.20E-05	0.00E+00	5.74E-04	2.15E-04	0.00E+00	7.67E-04

H2SO4 - 0 pCO2							
T (H)	Si (mol)	Al (mol)	Fe (mol)	Na (mol)	K (mol)	Mg (mol)	Ca (mol)
53	6.10E-04	3.31E-07	0.00E+00	7.03E-05	1.35E-04	0.00E+00	1.61E-04
118	1.30E-03	7.55E-06	1.79E-08	1.47E-04	2.19E-04	0.00E+00	3.62E-04
189	2.00E-03	1.55E-05	1.79E-08	2.25E-04	2.40E-04	0.00E+00	5.71E-04
238	2.46E-03	1.78E-05	1.79E-08	2.75E-04	2.57E-04	0.00E+00	7.13E-04
286	2.92E-03	2.34E-05	2.53E-08	3.24E-04	2.71E-04	0.00E+00	8.57E-04
315	3.20E-03	2.62E-05	5.77E-08	3.52E-04	2.81E-04	0.00E+00	9.41E-04
360	3.60E-03	3.14E-05	6.29E-08	3.93E-04	3.01E-04	0.00E+00	1.07E-03
406	4.01E-03	3.68E-05	6.29E-08	4.38E-04	3.15E-04	0.00E+00	1.20E-03
431	4.14E-03	3.93E-05	6.29E-08	4.53E-04	3.68E-04	0.00E+00	1.26E-03

HCl - 0 pCO2

T (H)	Si (mol)	Al (mol)	Fe (mol)	Na (mol)	K (mol)	Mg (mol)	Ca (mol)
46	3.71E-04	8.00E-07	2.19E-08	6.62E-05	5.90E-05	0.00E+00	1.10E-04
90	7.08E-04	1.58E-06	4.54E-08	1.08E-04	8.17E-05	0.00E+00	2.10E-04
162	1.26E-03	2.45E-06	6.32E-08	1.74E-04	1.53E-04	0.00E+00	3.77E-04
210	1.57E-03	3.00E-06	7.44E-08	2.08E-04	2.24E-04	0.00E+00	4.65E-04
258	1.91E-03	3.61E-06	9.44E-08	2.47E-04	2.61E-04	0.00E+00	5.59E-04
286	2.10E-03	4.97E-06	9.44E-08	2.69E-04	2.78E-04	0.00E+00	6.17E-04
334	2.45E-03	5.56E-06	9.44E-08	3.07E-04	2.99E-04	0.00E+00	7.21E-04
379	2.79E-03	6.21E-06	9.44E-08	3.39E-04	3.24E-04	0.00E+00	8.42E-04
430	3.11E-03	6.85E-06	2.96E-07	3.76E-04	3.64E-04	0.00E+00	9.36E-04

H2SO4 - 0.1 pCO2

T (H)	Si (mol)	Al (mol)	Fe (mol)	Na (mol)	K (mol)	Mg (mol)	Ca (mol)
27	4.23E-04	3.32E-06	3.47E-09	5.69E-05	3.23E-05	0.00E+00	7.78E-05
121	1.69E-03	1.47E-05	3.47E-09	1.92E-04	7.65E-05	0.00E+00	3.17E-04
200	2.86E-03	2.49E-05	3.47E-09	2.84E-04	1.66E-04	0.00E+00	5.26E-04
300	4.30E-03	4.02E-05	3.47E-09	3.99E-04	1.93E-04	0.00E+00	7.92E-04
350	5.02E-03	4.43E-05	1.47E-08	4.48E-04	2.09E-04	0.00E+00	9.28E-04
431	6.25E-03	4.66E-05	3.23E-08	5.26E-04	2.36E-04	0.00E+00	1.14E-03

Figure S1: SEM and EDS analysis of the original basalt. a. SEM image illustrating the basaltic glass, forsterite and inclusion of chromite. b. SEM image showing augite. c. qualitative EDS spectra of the minerals illustrated in a. and b.

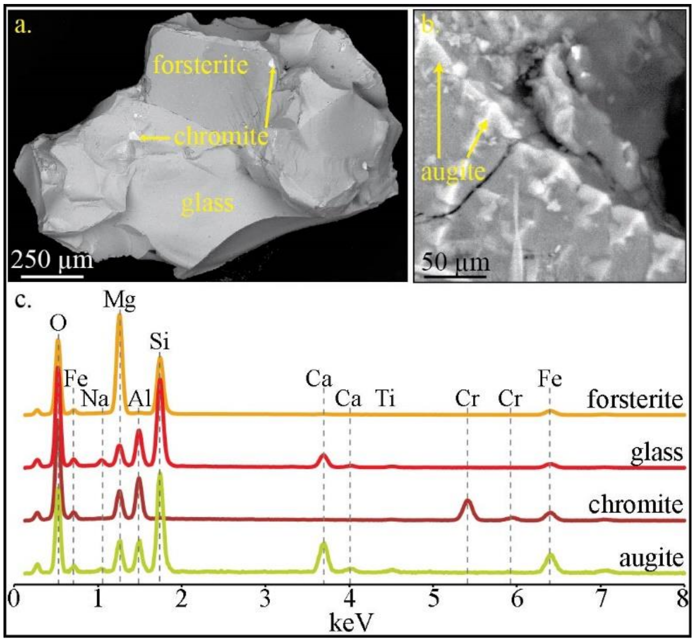

Figure S2: XRD patterns devoted to the 060 peak position of the unreacted and the reacted samples: a. pristine material, b. H2SO4 – 0.1 pCO2, c. H2SO4 – 0 pCO2, d. HCl – 0 pCO2, e. water – 0.1 pCO2 and f. water – 1-pCO2. The peak positions are labelled in Å.

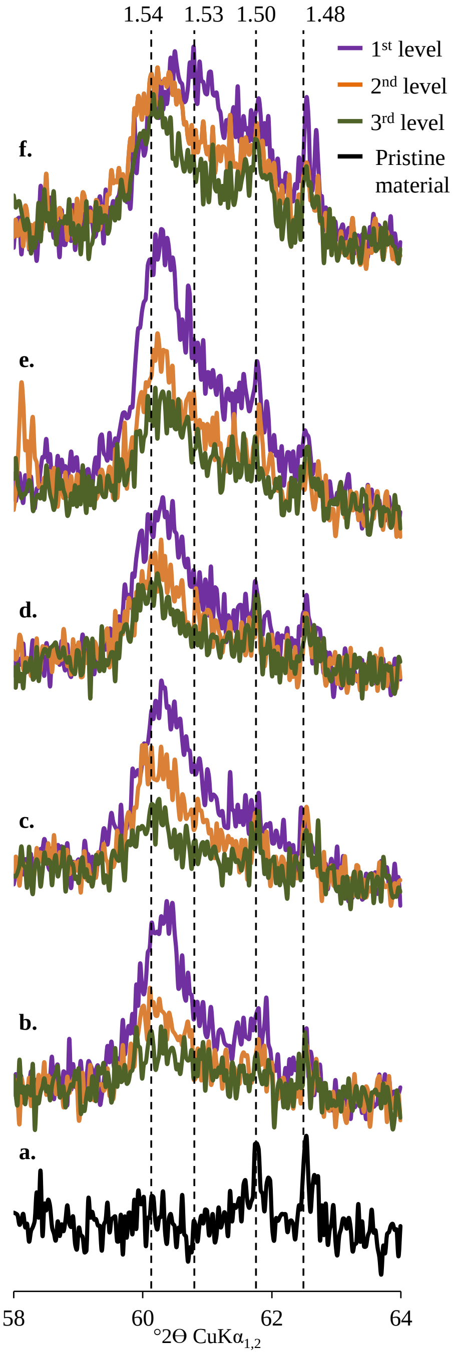

Supplementary results: clay minerals identification

The Figures S3, S4, S5, S6 and S7 present the XRD patterns obtained on oriented preparation devoted to the clay mineral analysis. As noticed in the bulk analysis, with the pCO_2 increase and the level # decrease, the contribution of the mixed-layer-mineral (MLM) at 7.22 Å in the Ca-AD state increases in disfavor of the MLM content at around 14-15 Å in the Ca-AD state. Similar XRD behavior as a function of the treatment can be observed with the different experiments or level #. Hence for simplification, the clay mineral identification will be described in detail by using the experiment where the contribution of the corresponding XRD peak is the most intense.

The identification of the MLM corresponding to the XRD peak at 7.22 Å in the Ca-AD state is performed for the water – 1 pCO_2 experiment (Figure S3). The XRD peak at 7.22 Å in the Ca-AD state shift slightly to 7.4 Å in the Ca-EG state, which is an indication of the presence of smectite layers. A slight shift towards higher angles between Ca-AD and K-AD state confirm their presence. Between K-AD, K-110, K-330 treatments, no differences can be observed. This is an indication that no Al-hydroxy interlayer layers are present even during the acidic conditions (Viennet et al., 2015). This XRD peak disappears after K-550 treatment. This XRD behavior could be the indication of kaolinite layers or of the 002 reflection of Fe-rich chlorite layers (Viennet et al., 2017). The NIR spectra figures 5 and 6 of the main manuscript do not show the presence of kaolinite layers with their characteristic bands at 2.16 and 2.2 µm. Hence, this MLM is a R0 MLM Fe-rich chlorite/smectite with a low amount of smectite layers. Between the Ca-AD and Ca-EG treatments, the XRD peaks shift between the experiments and the level #, which indicate that the smectite layer content is similar in the R0 Fe-rich chlorite/smectite MLM.

The nature of the MLM corresponding to the XRD peaks at around 14-15 Å in the Ca-AD state is identified for the HCl – 0 pCO_2 experiment (Figure S5). The XRD peak at 14.20 Å shift to 16.30 Å between the Ca-AD and Ca-EG treatments and the apparition of the 002 reflections at 7.52 Å show the presence of smectite layers. Between the Ca-AD, K-AD to K-550 treatments, the XRD peaks shift towards 10.62 Å. This behavior is attributed to the dehydration of water molecules in the interlayer space of the smectite layers with the temperature increase. The position and broad XRD peak after K-550 indicate that not only smectite layers compose such MLM but also chlorite layers to account for both the higher position than a pure smectite at ~10 Å and for mixed layering between ~10 Å and 14.2 Å layers, which broaden the XRD peak. Hence this MLM is a smectite-rich R0 MLM smectite/chlorite. Similar XRD behavior tendencies are noticeable for this MLM as a function of the experiments and the level # (Figures S2, S3, S4, S5 and S6). Nevertheless, noticeable differences can be observed on the peak intensities, width and shift between Ca-AD and Ca-EG treatments depending of the experiments considering. These differences can be related to the decrease of proportion and the lower coherent scattering domain size of such MLM with the pCO_2 increase and the level # decrease. Hence, in the water – 1 pCO_2 experiments, the shift between the XRD patterns at ~14.40 Å of the Ca-ED and Ca-EG states and between the Ca-AD and K-AD states indicates the presence of the R0 MLM smectite/chlorite; The low intensities and the large XRD peak show that this mineral low coherent scattering domain size. The XRD peaks at 7.22 Å in the Ca-AD state and 7.52 Å in the Ca-Eg state of the 0 pCO_2 experiments, show the presence of the R0 MLM Fe-rich chlorite/smectite.

Figure S3: XRD patterns recorded on oriented preparations devoted to the clay minerals identification as a function of the level # for the water – 1 pCO_2 experiment.

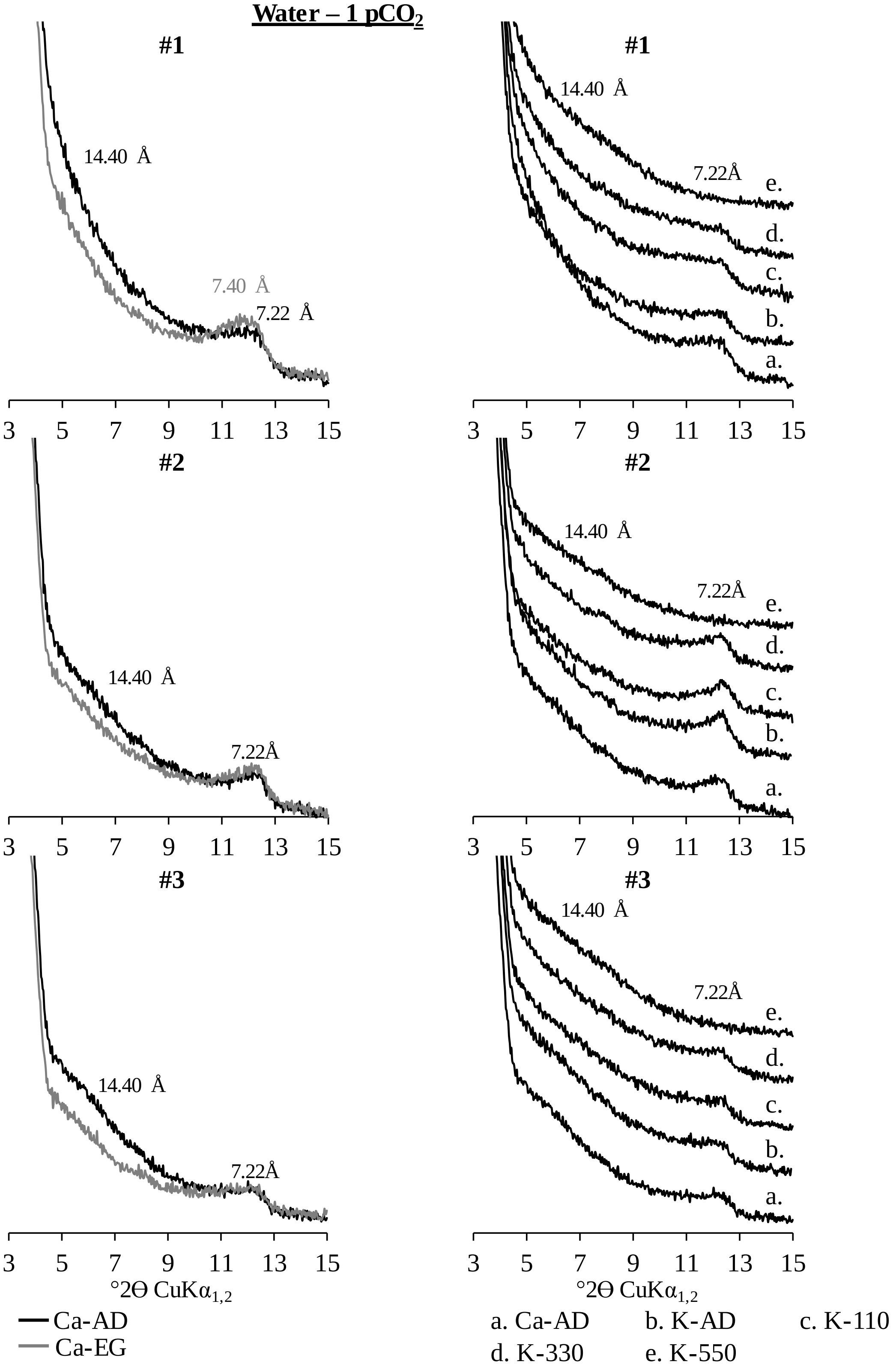

Figure S4: XRD patterns recorded on oriented preparations devoted to the clay minerals identification as a function of the level # for the water – 0.1 - pCO_2 experiment.

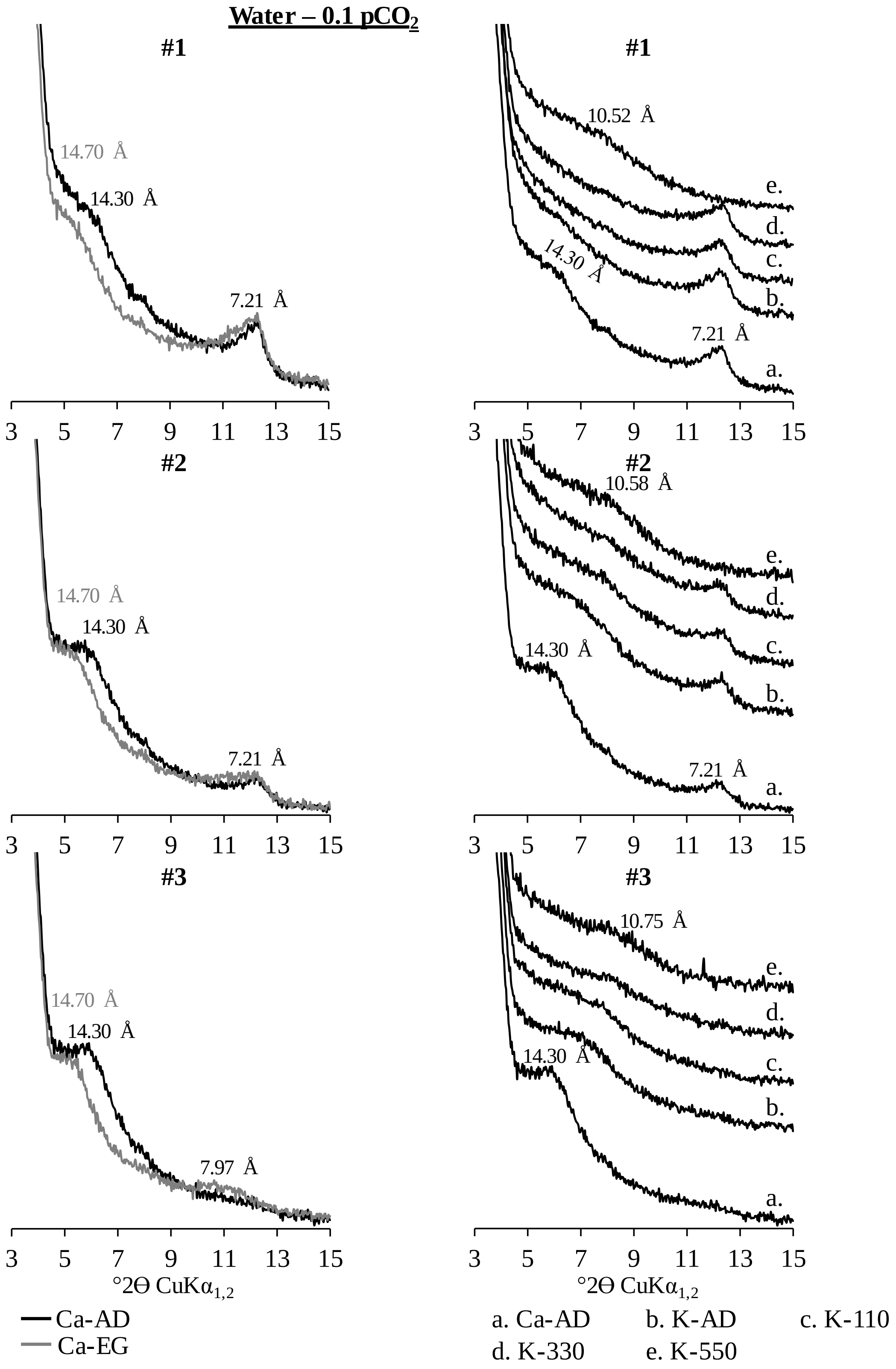

Figure S5: XRD patterns recorded on oriented preparations devoted to the clay minerals identification as a function of the level # for the HCl – 0 pCO_2 experiment.

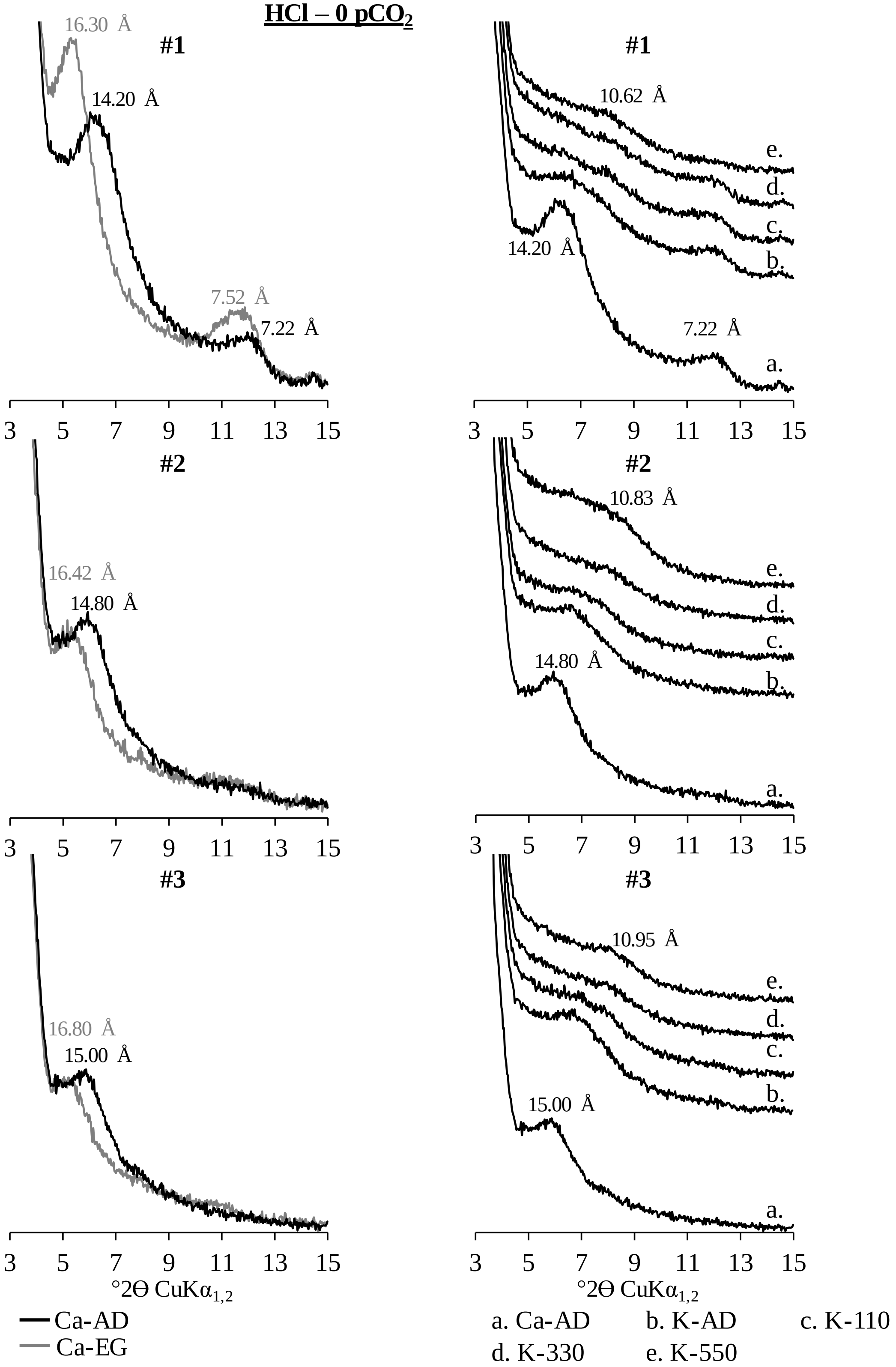

Figure S6: XRD patterns recorded on oriented preparations devoted to the clay minerals identification as a function of the level # for the H_2SO_4 – 0 pCO_2 experiment.

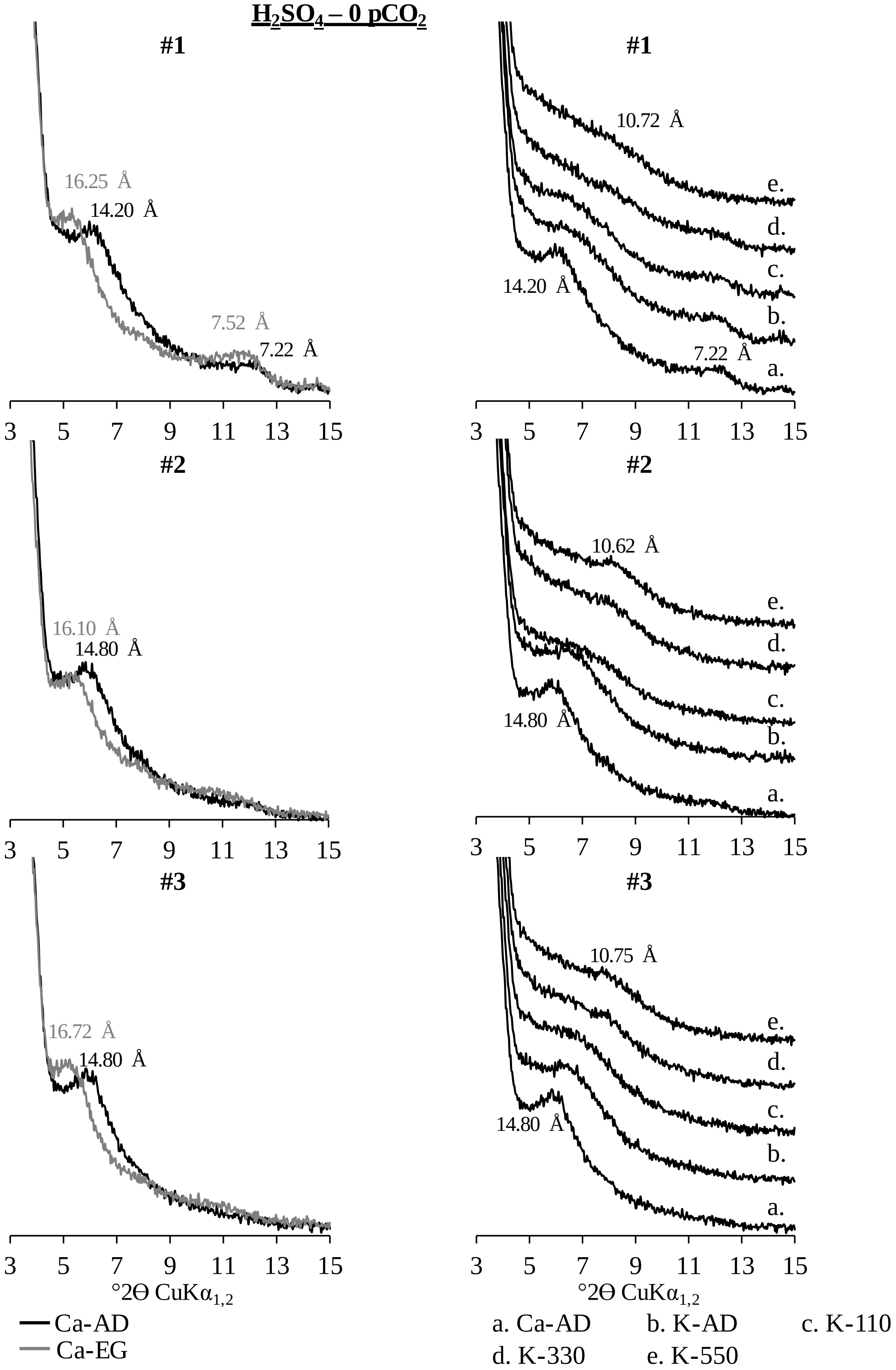

Figure S7: XRD patterns recorded on oriented preparations devoted to the clay minerals identification as a function of the level # for the H_2SO_4 – 0.1 pCO_2 experiment.

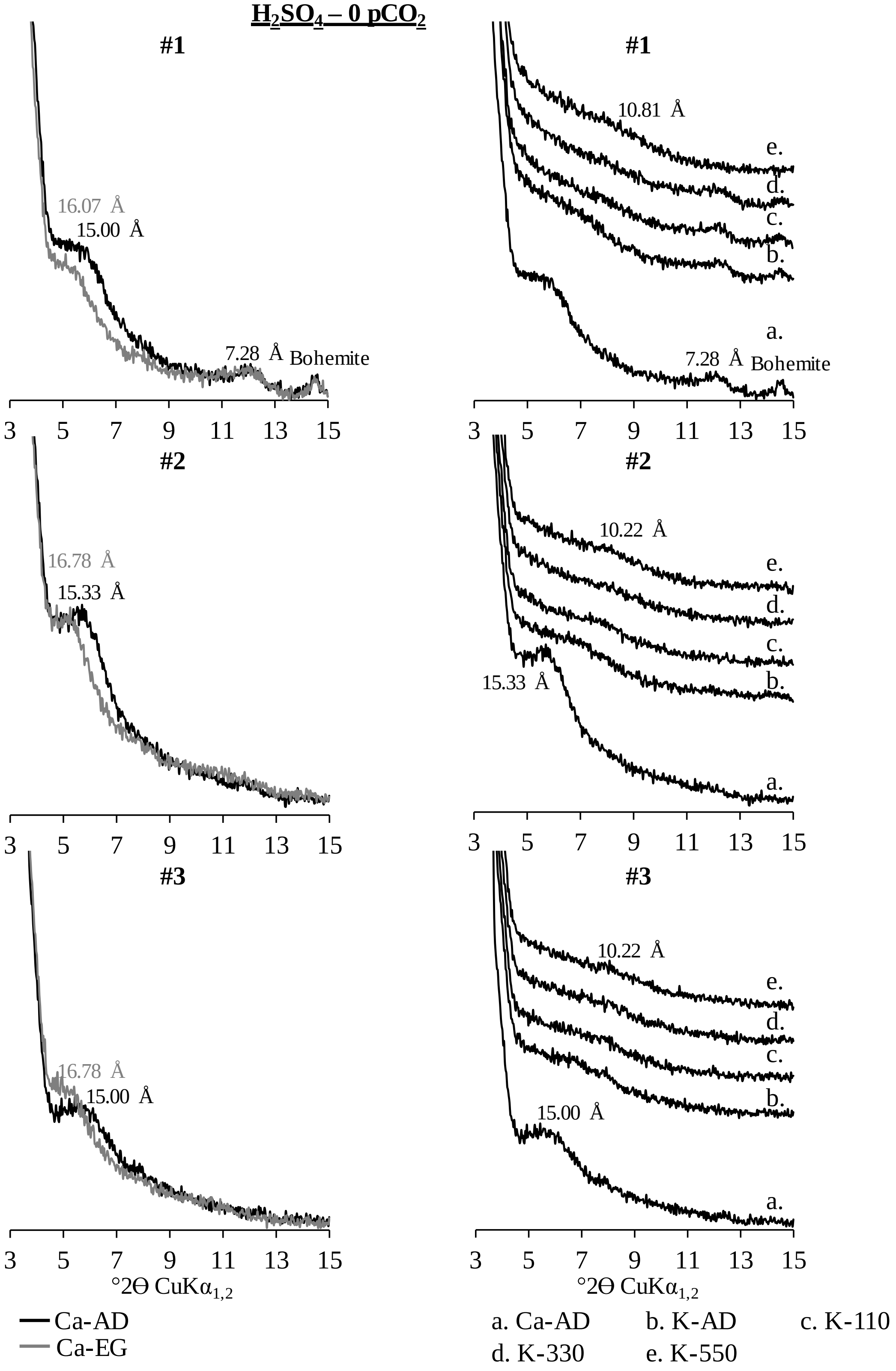

References

Viennet, J.-C., Bultel, B., Riu, L. and Werner, S.C. (2017) Dioctahedral phyllosilicates versus zeolites and carbonates versus zeolites competitions as constraints to understanding early Mars alteration conditions. Journal of Geophysical Research: Planets 122, n/a-n/a.

Viennet, J.-C., Hubert, F., Ferrage, E., Tertre, E., Legout, A. and Turpault, M.-P. (2015) Investigation of clay mineralogy in a temperate acidic soil of a forest using X-ray diffraction profile modeling: Beyond the HIS and HIV description. Geoderma 241, 75-86.